Sensitivity of Idealized Squall Line Simulation to Resolution and Subgrid Turbulence Mixing

by

Kwan Tsaan Lai

A thesis
presented to the University of Waterloo
in fulfillment of the
thesis requirement for the degree of
Master of Mathematics
in
Applied Mathematics

Waterloo, Ontario, Canada, 2019

Author's Declaration

I hereby declare that I am the sole author of this thesis. This is a true copy of the thesis, including any required final revisions, as accepted by my examiners.

I understand that my thesis may be made electronically available to the public.

Abstract

In this project, the sensitivity of idealized squall line simulations to horizontal grid spacing and turbulent mixing parameterization will be discussed. Inconsistent results from numerical simulations of convective systems have suggested that there are issues with the behaviour of the subgrid turbulent mixing parameterizations with increasing resolution that still need to be resolved. The Weather Research and Forecasting Model (WRF) will be used to perform large eddy simulations of idealized squall lines with horizontal grid spacings of 4 km, 1 km, 500 m and 250 m. A common background sounding profile is used so that simulations from this project can also be compared with other studies in the literature. The dependence of various squall line characteristics on the resolution, including cloud top height and mass flux, turbulence kinetic energy, energy spectra and backscatter will be discussed. In particular, we find that 4 km grid spacing is not recommended for simulations with explicit convection as it contains an unreasonable amount of subgrid turbulence kinetic energy and it is not able to resolve the large energy containing eddies. A significant amount of backscatter exists in at filter scales of $\Delta x = 4$ km and even 1 km, which is ignored by the eddy viscosity model.

Acknowledgements

First of all, I would like to sincerely thank my supervisor, Michael Waite. This thesis would not have been possible without him. I am very thankful for all the supports in the two years of my master time. Thank you for the patience and guidance. I hope all is well with Mike and his family.

I would like to thank my committee members, Marek Stastna and Francis Poulin, for their time and help.

I would also like to thank my friends and my family for their unconditional love and support.

Lastly, I would like thank the love of my life, Anni Wang. Thank you for being in my life.

This research was enabled in part by support provided by Sharcnet (www.sharcnet.ca) and Compute Canada (www.computecanada.ca).

Dedication

This is dedicated to the one I love.

Table of Contents

List of Tables

List of Figures

Chapter 1

Introduction

Atmospheric science is a fascinating research area. In particular, natural hazards such as storms have attracted lots of attention due to the damage that they cause to human society. Such storms are difficult and computationally expensive to model because of their turbulent nature. Squall lines are groups of thunderstorms which organize linearly. In this thesis, we investigate the sensitivity of idealized squall line simulations to resolution and subgrid turbulence mixing. We begin in this chapter by introducing the preliminaries for understanding the thesis: basic fluid mechanics, water vapour thermodynamics, microphysics parameterisation and large eddy simulations.

1.1 Fluid Mechanics

To understand the dynamics of a squall line, it is helpful to review the fundamental equations of fluid mechanics, which describe the motion of air in the atmosphere.

1.1.1 Material Derivative and Reynolds Transport Theorem

In order to understand the time derivative for a flowing fluid, the concept of material derivative and the time derivative of volume integral are introduced. The material derivative D/Dt [19] is defined as the rate of change seen by the fluid moving with velocity $\boldsymbol{u}$, and is given by

$$\frac{D}{Dt} = \frac{\partial}{\partial t} + \boldsymbol{u} \cdot \boldsymbol{\nabla}.$$

Consider the time derivative of the volume integral of a scalar field F [19],

$$\frac{d}{dt}\int_{V(t)} F dV,$$

where $V(t)$ is a material volume of the fluid. Then by the Reynolds Transport Theorem [19],

$$\frac{d}{dt}\int_{V(t)} F dV = \int_{V(t)} \frac{\partial F}{\partial t} + \boldsymbol{\nabla}\cdot(F\boldsymbol{u})\, dV. \tag{1.1}$$

1.1.2 Continuity Equation

By conservation of mass, the mass of a material volume should be constant over time. One can derive the continuity equation, which describes conservation of mass, using the Reynolds Transport Theorem (1.1) as follow:

$$0 = \frac{d}{dt}\int_{V(t)} \rho dV \tag{1.2}$$

$$= \int_{V(t)} \frac{\partial \rho}{\partial t} + \boldsymbol{\nabla}\cdot(\rho\boldsymbol{u})\, dV. \tag{1.3}$$

As a result, because (1.2) holds true for all material volumes, the integrand must be zero, which gives

$$\frac{\partial \rho}{\partial t} + \boldsymbol{\nabla}\cdot(\rho\boldsymbol{u}) = 0, \tag{1.4}$$

which can also be written as

$$\frac{D\rho}{Dt} = -\rho\boldsymbol{\nabla}\cdot\boldsymbol{u}.$$

1.1.3 Momentum Equation

The conservation of momentum can be obtained in a similar way. With the consideration of the forces acting on the fluid, the momentum equation is given by [19]

$$\rho\frac{Du_i}{Dt} = \rho g_i + \frac{\partial \tau_{ij}}{\partial x_j}, \tag{1.5}$$

where ρg_i is the gravitational force and τ_{ij} is the stress tensor, which gives the i-th component of the stress on the fluid with outward normal in the j-th direction [19]. The constitutive equation for Newtonian fluid is given by

$$\tau_{ij} = -p\delta_{ij} + 2\mu s_{ij} + \lambda \boldsymbol{\nabla} \cdot \boldsymbol{u}\delta_{ij}, \tag{1.6}$$

where

$$s_{ij} = \frac{1}{2}\left(\frac{\partial u_i}{\partial x_j} + \frac{\partial u_j}{\partial x_i}\right)$$

is the rate of strain tensor, δ_{ij} is the Kronecker delta, μ is the dynamic viscosity and λ is the bulk viscosity. The constitutive equation gives a description of how pressure and viscous force act on the fluid. In this thesis, viscosity will be neglected because the Reynolds number is very large, and hence viscous effects are small at the scales of interest.

1.1.4 Energy Equation for Dry Air

The equation of state for an ideal gas is given by [32]

$$p\alpha = R^{'}T, \tag{1.7}$$

where $\alpha = 1/\rho$ is the specific volume, $R^{'} = 287$ J kg^{-1}K^{-1} is the individual gas constant, p is the pressure and T is the temperature. According to the first law of thermodynamics, heat is a form of energy, and energy is conserved. Therefore,

$$dU = dQ - dW,$$

where dU is the change in internal energy of the system ($du = dU$ per unit mass), dQ is the heat added to the system ($dq = dQ$ per unit mass) and $dW = pdV$ is the work done by the gas, where V is the volume of the gas. The relation can be expressed for a unit of mass of gas [32],

$$du = dq - pd\alpha. \tag{1.8}$$

So,

$$dq = c_v dT + pd\alpha, \tag{1.9}$$
$$= c_p dT - \alpha dp, \tag{1.10}$$

where $c_v = 718$ J kg^{-1}K^{-1} is the specific heat at constant volume and $c_p = 1005$ J kg^{-1}K^{-1} is the specific heat at constant pressure.

The potential temperature θ is derived from the following: first, assume that the process is adiabatic (i.e. $dq = 0$). Then, using the equation of state and integrating (1.10) gives

$$\frac{T}{T_0} = \left(\frac{p}{p_0}\right)^k, \tag{1.11}$$

where T is the temperature at pressure p, T_0 is the temperature at pressure p_0, and

$$k = \frac{R^{'}}{c_p} = \frac{c_p - c_v}{c_p} = 0.286.$$

The potential temperature θ is the temperature of a parcel of air, with initial temperature T and pressure p, after it goes through an adiabatic process and reaches pressure of p_0 (usually 100 kPa) [32], and it is defined by (1.11),

$$\theta = T\left(\frac{p_0}{p}\right)^k. \tag{1.12}$$

The energy equation of dry air can therefore be expressed as [38]

$$\frac{Dln(\theta)}{Dt} = \frac{\dot{Q}}{Tc_p},$$

where $\dot{Q}$ is the rate of heating (e.g. heat diffusion).

1.1.5 System of Equations for Dry Air

In summary, the set of equations for dry air is given by

$$\frac{\partial \rho}{\partial t} + \boldsymbol{\nabla}\cdot(\rho \boldsymbol{u}) = 0, \tag{1.13a}$$

$$\rho\frac{Du_i}{Dt} = \rho g_i + \frac{\partial p}{\partial x_j}, \tag{1.13b}$$

$$\frac{D\theta}{Dt} = 0, \tag{1.13c}$$

$$\theta = T\left(\frac{p_0}{p}\right)^k. \tag{1.13d}$$

$$p = \rho R^{'} T. \tag{1.13e}$$

Note that $\dot{Q} = 0$ in the equation for dry air as heat diffusion is neglected. As we will see in later sections, as phase changes of water occur in the dynamics, the effect of latent heating will also be considered and appropriate consideration of $\dot{Q}$ will be taken.

1.2 Moist Fluid Dynamics

1.2.1 Water Vapour Thermodynamics

Water is present in the atmosphere in different phases, which modifies the equation in the previous section on dry air. First, we consider the thermodynamics of water vapour in unsaturated air. Note that water vapour can be considered as an ideal gas.

The equation of state for water vapour is [32]

$$e = \rho_v R_v T = \rho_v \frac{R^{'}}{\epsilon} T, \tag{1.14}$$

where $\epsilon = R_v/R^{'} = 0.622$ and $R_v = 461.5$ J kg^{-1}K^{-1} is the individual gas constant for water vapour.

Moist air is a mixture of dry air and water vapour. The mixing ratio q is defined as the mass of water vapour per unit mass of dry air and is given by [32]

$$q = \frac{\rho_v}{\rho_d} \tag{1.15}$$

$$= \epsilon \frac{e}{R'T} / \frac{p-e}{R'T} \tag{1.16}$$

$$\approx \epsilon \frac{e}{p}, \tag{1.17}$$

where ρ_d is the density of dry air and ρ_v is the density of vapour. Also note that the density of the air parcel contain both dry air and vapour, which is given by $\rho = \rho_d + \rho_v$.

The pressure of moist air p is the sum of the pressure of the dry air p_d and the pressure of

water vapour e [32]:

$$p = p_d + e \tag{1.18a}$$

$$= \rho_d R^{'} T + \rho_v \frac{R^{'}}{\epsilon} T \tag{1.18b}$$

$$= \rho_d R^{'} T \left(1 + \frac{q}{\epsilon}\right) \tag{1.18c}$$

$$= \rho R^{'} T \left(\frac{1 + \frac{q}{\epsilon}}{1 + q}\right). \tag{1.18d}$$

$$\tag{1.18e}$$

Note that (1.18d) resembles the ideal gas law for dry air with a modified temperature

$$T_v = T \left(\frac{1 + q/\epsilon}{1 + q}\right). \tag{1.19}$$

T_v is called the virtual temperature, and it is the temperature that dry air must have to have the same density as moist air. By using the concept of virtual temperature, the equation of state for dry air can also apply to moist, unsaturated air by replacing the original parcel temperature T with T_v [32].

1.2.2 Liquid Phase and Saturation

Some understanding of the saturation of moist air is necessary for the discussion in the rest of this chapter.

The pressure of saturated moist air can be used to determine if the air parcel is saturated. The saturation vapour pressure $e_s(T)$ gives the maximum vapour pressure at which water can be present in vapour form. For $e > e_S$, vapour will condense to liquid form. For $e < e_s$, water in liquid form will evaporate. An important equation for describing the pressure for saturated moist air is the Clausius-Clapeyron equation. The Clausius-Clapeyron equation for an ideal gas is given by [32]

$$\frac{de_s}{dT} = \frac{Le_s}{R_v T^2}, \tag{1.20}$$

where L is the latent heat of vapourisation.

The solution of the Clausius-Clapeyron equation tells us the saturation pressure e_s at a given temperature. This relation can be used to determine if the moist air in the atmosphere is saturated.

The dew point temperature T_d describes how close a sample of moist air is to saturation: holding mixing ratio q and pressure p constant, the dew point temperature is the temperature that the moist air has to be cooled to in order to be saturated [32].

1.3 Microphysics

Microphysics parameterisations are important parts of cloud resolving models that represent the effects of water phase changes such as precipitation, latent heating and cooling. The following set of equations is a simple example with three species of water: vapour, cloud and precipitation (e.g. [12, 13]):

$$\frac{D\theta}{Dt} = \frac{L\theta_e}{c_p T_e}(C_d + E_p), \tag{1.21a}$$

$$\frac{Dq_v}{Dt} = -C_d - E_p, \tag{1.21b}$$

$$\frac{Dq_c}{Dt} = C_d - A_p - C_p, \tag{1.21c}$$

$$\frac{Dq_p}{Dt} = \frac{1}{\overline{\rho}}\frac{\partial(\overline{\rho}V_T q_p)}{\partial z} + A_p + C_p + E_p, \tag{1.21d}$$

where q_c is the cloud water mixing ratio, q_p is the precipitation mixing ratio, θ_e and T_e are the ambient potential temperature and the ambient temperature respectively. The E are the evaporation terms, the C are the condensation terms, and V_T is the terminal velocity for the precipitation. The sets of equations (1.21), combined with the equations for dry air (1.13) with the virtual temperature in (1.13 d,e), give a complete set of equations for moist air.

1.4 Parcel Buoyancy and Atmospheric Stability

The stability of the atmosphere is often crucial for the formation of a storm. As a result, it is important to understand how stability and parcel buoyancy affect the development of a storm. The dry adiabatic lapse rate Γ is the rate at which the temperature of an air parcel cools with increasing height as the air parcel rises adiabatically. It can be obtained

by the following [32]:

$$c_p dT = \frac{R^{'}T}{p} dp, \tag{1.22a}$$

$$\Gamma = -\frac{dT}{dz} \tag{1.22b}$$

$$= \frac{-R^{'}T}{c_p p} \frac{dp}{dz} \tag{1.22c}$$

$$= \frac{-R^{'}T}{c_p p} (-\rho^{'} g) \tag{1.22d}$$

$$= \frac{R^{'}T}{c_p p} \frac{pg}{R^{'}T^{'}} \tag{1.22e}$$

$$= \frac{g}{c_p} \frac{T}{T^{'}} \tag{1.22f}$$

$$\approx \frac{g}{c_p}, \tag{1.22g}$$

where $\rho^{'}$ and $T^{'}$ are the ambient density and temperature respectively. $T/T^{'} \approx 1$ because the parcel temperature is approximately equal to ambient temperature.

Stability of an air parcel refers to the response to small vertical displacements: if the parcel is forced back to its initial height, it is stable; if the parcel experiences no force, it is neutral; and if the parcel is forced away from its initial height, it is unstable. Consider an environment with ambient lapse rate $\gamma = -dT^{'}/dz$. The stability criteria for dry can be determined as the following [32]:

If $\gamma < \Gamma$, the parcel is stable.

If $\gamma > \Gamma$, the parcel is unstable.

If $\gamma = \Gamma$, the parcel is neutral.

A simple example can be used to explain the stability criteria. Suppose a parcel has the same temperature T as the ambient air. As the parcel rise by a height of Δz, the temperature of the parcel will be $T - \Gamma \Delta z$. For small Δz, the ambient temperature at the new height will be $T - \gamma \Delta z$. If $\gamma > \Gamma$, the parcel is warmer than the ambient temperature. As a result, the parcel will be positively buoyant, continue to rise and hence the parcel is unstable. A similar argument can be made for the other two cases.

The above criteria can be expressed in terms of the potential temperature. From (1.12),

$$dT = \frac{T}{\theta} d\theta + \frac{kT}{p} dp.$$

Then one can take the derivative of the above equation with respect to z and obtain

$$\frac{1}{\theta}\frac{\partial\theta}{\partial z} = \frac{1}{T}\frac{\partial T}{\partial z} - \frac{k}{p}\frac{\partial p}{\partial z}, \tag{1.23}$$

$$= \frac{1}{T}(\Gamma - \gamma). \tag{1.24}$$

Note that the stability criteria can be rewritten in terms of $\partial\theta/\partial z$ [32]:

If $\gamma < \Gamma$ or $\partial\theta/\partial z > 0$, the parcel is stable.

If $\gamma > \Gamma$ or $\partial\theta/\partial z < 0$, the parcel is unstable.

If $\gamma = \Gamma$ or $\partial\theta/\partial z = 0$, the parcel is neutral.

The buoyant force on an air parcel with unit mass can be described by [32]

$$F_B = g\left(\frac{\rho^{'} - \rho}{\rho}\right) = g\left(\frac{T - T^{'}}{T^{'}}\right), \tag{1.25a}$$

$$= \frac{d^2 z}{dt^2} = g\left(\frac{T - T^{'}}{T^{'}}\right). \tag{1.25b}$$

Using (1.25b), one can linearise $T(z)$ and $T^{'}(z)$ and obtain

$$\frac{d^2 z}{dt^2} = \frac{-g}{T}(\Gamma - \gamma)z = \frac{-g}{\theta}\frac{\partial\theta}{\partial z}z = -N^2 z, \tag{1.26}$$

where

$$N^2 = \frac{g}{\theta}\frac{\partial\theta}{\partial z},$$

is called the Brunt–Väisälä frequency with unit of inverse time. N is the frequency of oscillation or the growth rate of z under small displacements, depending on whether it is stable or unstable.

The stability of unsaturated moist air can be determined in the same way as the stability of dry air above when the virtual temperature is used. The stability of the saturated moist air has to be considered differently because latent heat is released when saturated parcels are lifted. The pseudoadiabatic process assumes that condensate is precipitated immediately [32]. The pseudoadiabatic (also known as the moist adiabatic) lapse rate can be derived following (1.22a) with phase changes included, which is $c_p dT - \alpha dp = -L dq_s$ [32]:

$$\Gamma_S = -\frac{dT}{dz} = \Gamma\frac{\left(1 + \frac{Lq_s}{R^{'}T}\right)}{\left(1 + \frac{L^2\epsilon q_s}{R^{'}c_p T^2}\right)}, \tag{1.27}$$

where q_s is the cloud water mixing ratio of saturated moist air. Note that L is the specific latent heat of condensation of water, and it is large, so $\Gamma_S < \Gamma$ and lifted saturated parcels cool less quickly than unsaturated parcels. The stability of moist unsaturated or saturated air is determined by the following:

If $\gamma < \Gamma_S$, the parcel is absolutely stable.

If $\gamma = \Gamma_S$, the parcel is saturated neutral.

If $\Gamma_S < \gamma < \Gamma$, the parcel is conditionally unstable.

If $\gamma = \Gamma$, the parcel is dry neutral.

If $\gamma > \Gamma$, the parcel is absolutely unstable.

Conditional instability means that unsaturated parcels are stable but saturated parcels are unstable.

1.5 Skew-T Diagram

Skew-T graphs are helpful in giving information about the stability of the environmental temperature and vapour profiles, which is closely related to the chance of having storms in the region [23].

Figure 1.1 is a typical Skew-T diagram (e.g. [32]). In the atmosphere, as height increases, the pressure will decreases. Because of that, the pressure on the y-axis can be viewed as the height. The brown solid horizontal grid lines are the lines of constant pressures (isobars). As such, the Skew-T graph can show the temperature of an air parcel as it rises. The pressure at sea level is about 1000 mb (1000 hPa) and it is also the pressure at the bottom of the Skew-T graph. The brown solid parallel grid lines from bottom left to top right are the lines of constant temperature (isotherms). The brown solid curved lines that go from the bottom right to the top left are the dry adiabatic curves. They represent how a dry parcel cools down if it is lifted adiabatically. The green solid curved lines are the moist adiabatic (pseudoadiabatic) curves, which give the temperature of a saturated parcel as it cools down pseudoadiabatically. The green dash lines are the constant saturated mixing ratio. The solid black line is the air temperature and the blue solid line is the dew point temperature.

The temperature and buoyancy of a conditionally unstable air parcel as it rises can be estimated from the red dashed line on the Skew-T graph as follows: a parcel, which has the temperature of the surrounding temperature given by the black solid line at sea level,

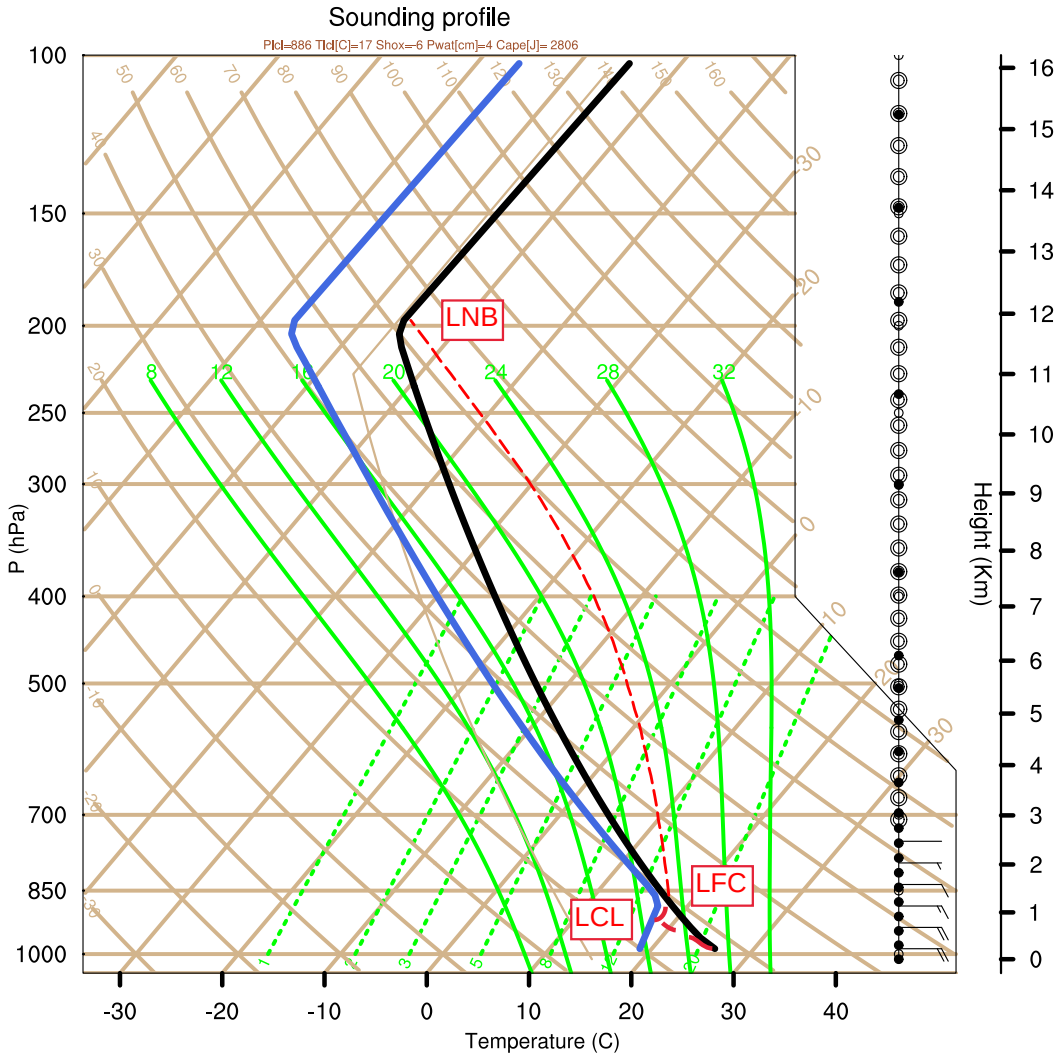

Figure 1.1: The Skew-T graph for this thesis. This is the sounding profile for this thesis, which is from Weisman and Klemp [44]. The black solid line is the air temperature, the blue solid line is the dew point temperature, the red dashed line is the temperature that a conditionally unstable air parcel will have as it rises. The brown solid horizontal grid lines are the isobars, the brown solid parallel grid lines from bottom left to top right are the isotherms, the brown solid curved lines that go from the bottom right to the top left are the dry adiabatic curve, the green solid curved lines to the left as going up are the moist adiabatic curve, and the green dash lines are the lines of constant saturated mixing ratio. The wind barbs on the right side of the plot show the wind speed and wind direction at the corresponding heights.

will follow the dry adiabat as it rises. As the parcel rises and its temperature intersects the dew point temperature (the height of this point known as the lifting condensation level, or LCL), it reaches saturation. With further lifting, the air parcel will follow the moist adiabat (green solid line) starting from this point as it rises. As the air parcel rises and intersects the air temperature curve (solid black curve), the air parcel becomes neutrally buoyant. This height is called the level of free convection. With further lifting, the air parcel is in an unstable condition and rises freely along the moist adiabat curve until it reaches to the level of neutral buoyancy (LNB), at which its temperature again intersects with the ambient temperature. The air parcel will not rise beyond the LNB unless force is applied to the air parcel. In real life, the parcel will not reach to the LNB because the parcel will mix with the environment as it rises, but the LNB is still a useful estimate of the maximum height attainable from moist convection.

The area on the Skew-T diagram between the parcel and the ambient temperature curves, between the lifting condensation level to the level of free convection, is called the convective inhibition energy (CIN). Similarly, the area from the LFC to LNB is called the convective available potential energy (CAPE) [23]:

$$CAPE = \int_{z_{LFC}}^{z_{LNB}} g\left(\frac{\theta - \overline{\theta}}{\overline{\theta}}\right) dz, \tag{1.28}$$

where z_{LNB} is the level of neutral buoyancy and z_{LFC} is the level of free convection. The CAPE gives a measure of the potential energy that can be released by an unstable air parcel, and therefore the strength of the convection.

1.6 Mesoscale Convective Systems

Mesoscale convective systems (MCS) are groups of thunderstorms which produce significant precipitation. Natural hazards are often associated with MCS. Hence, MCS have drawn lots of interests. MCS are often systems of storms with horizontal length scales of 10 km to 1000 km [23]. MCS can also be understood as groups of storms with horizontal length less than the Rossby radius of deformation, $L_R = NL_z/f$, where f is the Coriolis parameter and L_z is the characteristic vertical scale. Typically, $L_R \approx 1000$ km, with $N = 0.01$ s^{-1}, $L_z = 10$ km and $f = 10^{-4}$ s^{-1} [23].

There are three main types of convective systems: single cell, multicell and supercell storm [23]. A single cell storm is made up of a single updraft. The environmental wind shear is usually weak. As a result, the storm will be killed rapidly by evaporative cooling of the

precipitation which the storm creates [23]. A multicell storm is made up of a couple of convective cells. The environmental wind shear is usually strong, the precipitation region is offset from the convective updrafts, and hence the precipitation will not inhibit the updraft and kill the storm. As a result, a single cell storm usually can last for half an hour, while a multicell storm can last for a couple hours. A supercell storm has a large strong, rotating updraft which lasts for a long time [23]. The main difference between a supercell storm and the other two storms is that the main updraft of a supercell storm is rotating and hence the storm structure is different. A supercell storm often lasts for a couple hours.

A squall line is a kind of mesoscale convective system. It is a line of thunderstorms with significant precipitation, that propagates in the direction perpendicular to the line (e.g. [4]). Figure 1.2 shows a schematic drawing of a squall line. Squall lines are often associated with natural hazards such as strong wind, precipitation and ice storms. As a result, squall lines have been an active research topic for decades (e.g. [33]). A squall line can be classified by the environmental wind shear and the precipitation characteristics.

Environmental shear is important for the creation of a squall line. As a result, it is often used as a tool to classify a squall line. Two types of squall lines with different wind shear will be discussed: the deep shear model and shallow shear model. The squall line in the deep shear model tilts against the basic wind shear (forward tilted). Precipitation often occurs in the leading region and creates a downdraft due to evaporation [23]. Coherent circulation occurs due to the wind shear offsetting the downdraft region from the updraft region due to latent heating. The squall line in the shallow shear model is rearward tilted. The rearward tilted nature also means that the upper portion of the cloud of the squall line in the shallow shear model is above the cold pool and trailing behind [23]. The shallow shear model squall line is also known as California squall line. The rearward tilted squall line interacts with the cold pool associated with the precipitation and creates the rear-inflow jet.

The major difference between the squall line in the deep and shallow shear model is that the upper portion of the cloud of the squall line in the deep shear is tilting forward, while the upper portion of the cloud of the squall line in the shallow shear model is tilting backward. Such difference in the tilting direction of the squall line also affects the unloading of the precipitation. Hence, the precipitation of the squall line in the deep shear model is unloaded at the front of the updraft, while the precipitation of the squall line in the shallow shear model is unloaded at the back of the updraft.

Precipitation characteristics are also commonly used for classifying squall lines, in which a large region of stratiform precipitation (covering large area horizontally and not extending as much vertically) occurs with the squall line [23]. Trailing stratiform squall lines account

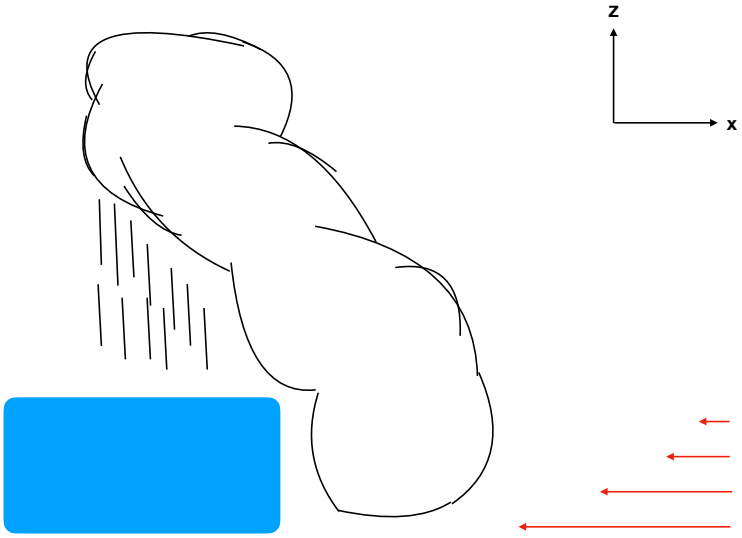

Figure 1.2: A schematic side view of a backward tilting squall line. The cloud is outlined in black, the blue region is the cold pool created by precipitation, and the red arrows show wind shear.

for 60% of squall lines, parallel stratiform squall lines account for 20% of squall lines, and leading stratiform squall lines account for 20% of squall lines [23]. The flow circulation for the leading stratiform squall line is similar to the flow circulation for the deep shear model squall line and the flow circulation for the trailing stratiform squall line is similar to the flow circulation for the shallow shear model squall line. Since trailing stratiform squall lines are the most common squall lines, they are the subject of this project.

Several conditions are necessary for the formation of a squall line [23]. First, an environment with sufficient conditional instability is necessary. Second, mechanical or thermal forcing which provides lifting to air parcels is required. Third, the presence of vertical shear is important for the maintenance of a squall line as described in the RKW theory section.

What makes the multicell storm such as the mesoscale convective system interesting is that it has a significantly longer duration time than a single cell storm. As a result, maintenance mechanisms are also important for understanding a squall line. Three-dimensional effects have been shown to be important for the propagation and maintenance of a squall line. Some studies ([7]) suggest that certain orientation of the wind shear with respect to the supercell storm is favourable for the maintenance of the storm. Moreover, the local balance mechanism is also important (see section 1.7).

1.7 RKW Theory

The importance of regions of cool air associated with evaporating precipitation, known as cold pools, and low level wind shear in the environment was initially overlooked by the community when trying to understand squall lines. The RKW theory, named after the three authors Rotunno, Klemp, and Weisman [33], suggests that storm generated cold pools and wind shear can affect the intensity of a squall line. It also describes how a squall line can reach its "optimal" state. The RKW theory [33] is a theory relating the local balance mechanism in a squall line with cold pools and low level shear. Cold pools and low level shear alone will kill the squall line, but combining cold pools and low level shear together will create a circulation.

In an environment without wind shear, cold pools are often considered as bad for the persistence of a convective system [33]. Rotunno et al. [33] suggested that cold pools would propagate away from the cloud and inhibit the lifting of warm, moist parcels at low levels. Cold pools, in general, are not favourable for strong updrafts in unsheared environment. Similarly, in an environment without a cold pool, a downshear tilted squall line is formed with low level environmental wind shear. The downshear tilted cloud produces a downdraft which inhibits the updraft.

The RKW theory describes the evolution of a squall line in an environment with low level wind shear in three stages. Rotunno et al. [33] defined the density current speed generated by the cold pool

$$c = \sqrt{-2Hg\Delta\theta/\theta_0},$$

where $\Delta\theta$ is the potential temperature difference from surrounding temperature θ_0, H is the height of the density current and ΔU is the low level wind shear. At the first stage, with no significant cold pool, the updraft is downshear titled ($c < \Delta U$). At the second stage, precipitation starts to form and cold pool develops due to evaporative cooling from the precipitation. At this stage, $c \approx \Delta U$ and the effect of the cold pool counters the effect of the wind shear and the updraft rotates upright. This stage is considered as the optimal state of the squall line. The squall line has the deepest convective lifting in this stage, and the updraft and downdraft circulations are balanced. At the last stage, as cold pool build up, the strength of the cold pool become stronger than the wind shear ($c > \Delta U$). The squall line becomes upshear tilted with trailing stratiform precipitation. The rear-inflow jet due to the circulation will generate a new cell and the squall line will be at this stage for the rest of its life.

1.8 Anelastic Approximation

While the main equations in this thesis are compressible, we will use the anelastic approximation in some post-processing. In the atmosphere, compressible effects apart from the decrease in density with height are small. As a result, the anelastic approximation can be used to simplify the set of governing equations. In the atmosphere, the variation of density, pressure and potential temperature at a certain height is often small compared to the balanced state [38]. Let

$$\rho = \widetilde{\rho}(z) + \rho'(x, y, z, t), \tag{1.29}$$
$$p = \widetilde{p}(z) + p'(x, y, z, t), \tag{1.30}$$
$$\theta = \widetilde{\theta}(z) + \theta'(x, y, z, t). \tag{1.31}$$

and assume $|\rho'| \ll \widetilde{\rho}(z)$.

Furthermore, continuity equation [38] takes the simpler form

$$\nabla \cdot (\widetilde{\rho}\,\boldsymbol{v}) = 0, \tag{1.32}$$

which is also known as the anelastic approximation. The set of equations for dry air become

$$\frac{D\boldsymbol{v}}{Dt} = \hat{\boldsymbol{k}} g \frac{\theta'}{\widetilde{\theta}} - \boldsymbol{\nabla}\left(\frac{p'}{\widetilde{\rho}}\right), \tag{1.33a}$$
$$\nabla \cdot (\widetilde{\rho}\,\boldsymbol{v}) = 0, \tag{1.33b}$$
$$\frac{Dln(\theta)}{Dt} = \frac{\dot{Q}}{Tc_p}, \tag{1.33c}$$

The θ equation will be discussed in the next section.

1.9 Large Eddy Simulations

Large eddy simulations (LES) is a computational technique used in turbulent simulations (e.g. [30, 46]). Small scale eddies are expensive to resolve computationally. As a result, by resolving the large energy containing eddies and parameterising the effect of small scale eddies, one can simulate a turbulent with less computational power.

Large eddy simulations is useful because, given the limited resources in computation power, it is impossible to resolve down to molecular viscous scales (e.g. [9, 46]). As a result, we have to parameterise subgrid turbulence mixing and this is done by filtering the equations of motion (e.g. [9, 46]).

Consider the filter

$$\overline{u_i} = \iiint u_i(\boldsymbol{x}')G(\boldsymbol{x}-\boldsymbol{x}')dx_1'dx_2'dx_3',$$

where G is a filter function. For large eddy simulations, the viscous term in Navier-Stokes equation is small compared to other terms, since Reynolds number for turbulence is huge. So the filtered momentum equation is

$$\frac{\partial \overline{u_i}}{\partial t} + \frac{\partial(\bar{u}_i\bar{u}_j)}{\partial x_j} = \frac{-1}{\rho}\frac{\partial \overline{p}}{\partial x_i} - \frac{\partial \widetilde{\tau_{ij}}}{\partial x_j}, \tag{1.34}$$

where $\widetilde{\tau_{ij}} = \overline{u_iu_j} - \bar{u}_i\bar{u}_j$. $\widetilde{\tau_{ij}}$ is introduced for modeling the subgrid turbulence mixing with a viscosity-like term. It is common to work with a modified version of the filtered conservation equation.

$$\frac{\partial \overline{u_i}}{\partial t} + \frac{\partial(\bar{u}_i\bar{u}_j)}{\partial x_j} = -\frac{\partial(\overline{p}/\rho + 2e/3)}{\partial x_i} - \frac{\partial \tau_{ij}^d}{\partial x_j}. \tag{1.35}$$

where

$$\tau_{ij}^d = \overline{u_iu_j} - \bar{u}_i\bar{u}_j - \frac{2}{3}e\delta_{ij}$$

and

$$e = \frac{1}{2}(\overline{u_iu_i} - \bar{u}_i\bar{u}_i).$$

As we can see in the later section on subgrid turbulence mixing scheme, the eddy viscosity model can be used to parameterise τ_{ij}^d using the eddy viscosity K:

$$\tau_{ij}^d = K\overline{s_{ij}}, \tag{1.36}$$

where $\overline{s_{ij}}$ is the filtered rate of strain.

1.10 Subgrid Turbulence Mixing Scheme

The more accurate subgrid turbulence is represented by the model, the more accurate the simulated storm will be. As a result, the subgrid turbulence mixing scheme is fundamentally important to the outcome of the simulation. Two basic subgrid turbulence mixing

schemes, the Smagorinsky scheme ([36]) and the turbulence kinetic energy (TKE) closure model (e.g. [30, 46]), will be introduced in this section.

Lilly and Smagorinsky suggested the eddy viscosity model (e.g. [36]) in the 1960s. The smallest eddies are too expensive to resolve directly. As a result, those eddies can be modelled by a viscosity-like term in the momentum equations. The eddy viscosity model assumes that the large energy containing eddies are transferring energy to smaller eddies, and eventually dissipate the energy to unresolved scales, which is also known as the energy cascade assumption for large eddy simulation (e.g. [30, 46]). The eddy viscosity model assumes that the flow is turbulent and the grid spacing used is able to resolve the large energy containing eddies but not the eddies in the dissipation range. The dissipation range can be estimated using the Kolmogorov scaling (e.g. [30, 46]). For this project, the size of the energy dissipating eddies is on the order of millimetres. Whether or not the grid spacings used in this project are able to satisfy the above assumptions will be discussed.

The Smagorinsky model proposes that the eddy viscosity K [36] is determined entirely by the filtered strain rate, and given by

$$K = \frac{(k\Delta D)^2}{\sqrt{2}}, \tag{1.37}$$

where

$$D^2 = \overline{s_{ij}}\,\overline{s_{ij}}, \tag{1.38}$$

Δ is the grid spacing, and $k \approx 0.17$ is proposed by Lilly [21].

Another commonly used eddy-viscosity model is the turbulence kinetic energy (TKE) closure model. The TKE closure model takes the turbulence kinetic energy into consideration when it is modelling the subgrid mixing. As a result, it is considered as an improvement to the Smagorinsky scheme. The eddy viscosity K for the turbulence kinetic energy (TKE) closure model is defined as

$$K = C_u e^{1/2} \Delta, \tag{1.39}$$

where $C_u = 0.15$ [35] is a constant, and $e = (u_i - \overline{u_i})(u_i - \overline{u_i})/2$ is the subgrid TKE. Note that e is not directly resolved in large eddy simulations, and is predicted by an approximate parameterised equation [21, 46]. Also note that TKE is used in this thesis to refer to two different ways: the TKE scheme, which is the eddy viscosity closure (1.39), and the TKE field, which is the kinetic energy of the turbulent part of the velocity field. The TKE field usually refers to the subfilter TKE e.

1.11 Literature Review

Convective systems have been studied for many years, and great progress has been made in understanding them (e.g. [14]). Numerical simulation is an efficient way of investigating and testing hypotheses about convective systems. Collecting storm data in field campaigns is difficult, dangerous and costly (e.g. [5]). As a result, idealized storm simulation is a cost-effective way of investigating storms. Squall lines are a great choice of idealized convective system for study because they have been the subject of many different investigations, with which the current study can be compared (e.g. [22, 33]). Lilly [22] summarized the technique and set up the basic model equations for large eddy simulation of convective flows, presented two-dimensional and three-dimensional simulations of a squall line, and discussed the effect of shear. Early successes in storm simulations have inspired research in different aspects of cloud resolving model (CRM) and large eddy simulation (LES) of mesoscale convective systems, including squall lines, such as the effect of horizontal and vertical resolution (e.g. [20]), environmental instability (e.g. [31, 27]), microphysics parameterisation (e.g. [8, 27]), vertical wind shear (e.g. [3]), subgrid turbulence mixing scheme (e.g. [39, 40]), cold pool dynamics (e.g. [34]), environmental humidity (e.g. [15]) and surface conditions (e.g.. [28]) on storm simulations.

The effect of the resolution on simulations of mesoscale convective systems is significant (e.g. [45, 6, 9, 11, 8, 20, 39]). Low resolution can lead to significant delay of storm development (e.g. [45, 9, 8]). Sub-kilometer horizontal resolution is necessary for capturing the convective structures of the systems (e.g. [8, 39]). These overall conclusions have been demonstrated in many studies.

Weisman et al. [45] investigated the effect of horizontal resolution on convective systems using a nonhydrostatic cloud model with horizontal grid sizes from 12 km to 1 km. They concluded that 4 km of grid spacing was sufficient to resolve the mesoscale structure of the convective system that was produced in the 1 km simulation.

Bryan et al. [9] conducted squall line simulations with four different grid spacing between 1 km to 125 m. As resolution increases, the convergence of results did not occur. Their results suggested that simulations with 1 km grid spacing contained an unrealistically large amount of subgrid turbulence energy. As a result, simulations with 1 km grid spacing should not be used as the benchmark for lower resolution simulations. Instead, simulation with a grid spacing of O(100) m should be used. Bryan and Morrison [8] conducted idealized squall line simulations with horizontal resolutions of 250 m, 1 km and 4 km and different microphysics parameterisations. They showed that the effect of horizontal resolution was more significant than that of microphysics parameterisation. The cloud top

height in the 1 km run was higher than in the 4 km run or 250 m run, suggesting that the cloud top height results from a competition between resolved and subgrid turbulence mixing (consistent with other studies (e.g. [42])). In a similar study, Morrison et al. [27] compared idealized deep convective storm simulations with horizontal grid spacing between 125 m to 2 km, three different environmental soundings, and three different microphysics parameterisation. They showed that sensitivity of the storm to horizontal resolution does not strongly affect precipitation, evaporation and condensation. They also suggested that differences in cloud water evaporation and temporally averaged surface precipitation as resolution increased from 1 km to 250 m with Bryan and Morrison [8] may be related to the different sounding profile and wind shear. Lebo and Morrison [20] conducted idealized simulations of squall lines with seven different horizontal resolutions from 33.33 m to 2 km and vertical resolutions of 500 m and 250 m. They found that decreasing the horizontal grid spacing to below 250 m did not change convective characteristics such as the mean number and area of convective cores.

In addition to examining the dependence of simulated storm characteristics on grid spacing, some studies have considered the behaviour of sub-grid turbulence parameterisations at different resolutions. Verrelle et al. [39] conducted multicellular storm system simulations with grid spacings of 4 km, 2 km, 1 km, 500 m. They showed that the ratio of subgrid turbulence kinetic energy to the total turbulence kinetic energy increases as the resolution increases. This finding is consistent with earlier work (e.g. [2]). However, Bryan et al. [9] found that the ratio of subgrid turbulence kinetic energy to the total turbulence kinetic energy decreases as the resolution increases. Similarly, Potvin and Flora [31] conducted idealized supercell simulation with horizontal resolution from 333 m to 4 km. They suggested that horizontal resolution of 1 km could produce a useful forecast, but benefits could be seen when horizontal resolution was further increased to 333 m. Verrelle et al. [40] had an interesting approach towards the topic. They conducted LES of a deep convective cloud with 50 m horizontal grid spacing, then they filtered subgrid turbulence field to 500 m, 1 km and 2 km. They suggested that thermal effects dominate at resolution of 2 km and 1 km and dynamical effects dominate at a resolution of 500 m or higher.

The effect of subgrid turbulence mixing schemes on simulations of mesoscale convective systems is significant (e.g. [37, 26, 18]). Takemi and Rotunno [37] investigated the effect of subgrid mixing scheme and numerical filter on squall lines with no shear and strong shear. They suggested eddy viscosity value for the Smagorinsky and TKE mixing schemes. Moeng et al. [26] performed a test with a mixed subgrid turbulence scheme with two newly added terms in the subgrid scale flux on a tropical deep convection system. The representation of subgrid scale fluxes of heat, moisture and momentum improved with the mixed subgrid scheme and horizontal grid spacing of a few kilometres. Kirkil et al. [18]

simulated neutral atmospheric boundary layer flows over a flat terrain and a ridge with Smagorinsky, Lagrangian-averaged scale-dependent dynamic, nonlinear backscatter and anisotropy and dynamic reconstruction model mixing scheme. The Lagrangian-averaged scale-dependent dynamic and dynamic reconstruction model was found to be more accurate than Smagorinsky mixing and nonlinear backscatter model, but also took $25 - 28\%$ more CPU time than Smagorinsky mixing scheme to compute.

While the vertical resolution has an effect on simulations of mesoscale convective systems, some studies have found that the storms are qualitatively similar for minimum vertical resolutions of 200 m to 50 m(e.g. [2, 20, 41]). Adlerman and Droegemeier [2] simulated a cyclic mesocyclone, which is a type of supercell storm. They found that decreasing the minimum vertical resolution from 200 m to 50 m would speed up the cycling process, but that the simulated storms were qualitatively similar. Since our minimum vertical grid spacing is similar, the dependence on vertical resolution will not be discussed in this thesis.

In general, there is agreement among these studies that sub-kilometre resolution is necessary in order to properly resolve mesoscale convective systems, like squall lines (e.g. [9, 8, 39]). However, several questions remain about the sensitivity and robustness of LES of squall lines. Inconsistencies between cited studies in area such as subgrid TKE ratio as resolution increase (e.g. [2, 9, 39]) and cloud water evaporation and temporally averaged surface precipitation as resolution increase (e.g. [8, 27]) have been shown.

1.12 Objectives

In this thesis, we will try to address the following questions: How sensitive are idealized squall line simulations to horizontal resolution and subgrid turbulence mixing? Is there an optimal resolution for balancing accurate forecasting and computational power? Are there any agreements or disagreements with the literature, such as the dependence of the ratio of subgrid turbulence kinetic energy to total turbulence kinetic energy with the resolution increase (e.g. [2, 9, 39])?

A total of 12 simulations of idealized squall lines are presented in this thesis, which is a combination of 4 horizontal resolutions and 3 subgrid turbulence mixing schemes. The effects of horizontal resolution and subgrid turbulence mixing scheme on characteristics such as the structure of the simulated squall line, subfilter energy transfer rate and subgrid turbulence kinetic energy are examined in this thesis.

Methodology, including a description of the WRF model [35] and simulations, is given in the next chapter.

Chapter 2

Methodology

The University of Waterloo is a member of SHARCNET (www.sharcnet.ca), a consortium of 18 universities and colleges operating a network of high-performance compute clusters in south western, central and northern Ontario. The Graham cluster is used for the simulations of this project. The high performance computing details can be found in the appendix section. In this section, a brief description of WRF, the set up of the simulations and the diagnostic will be discussed.

2.1 WRF

The Weather Research and Forecasting model (WRF) is used in this thesis. It is a great tool for cloud resolving and large eddy simulations. Many options such as microphysics and surface physics parameterisations are available to choose from. WRF can be used for idealized simulations and simulations with real data. The WRF model is well supported by the community and details of the model are well-documented. More details on WRF can be obtained from the WRF technical manual [35].

WRF solves the fully compressible, nonhydrostatic Euler equations [35]. It uses a third order Runge-Kutta scheme in time, third order advection scheme in vertical and fifth order advection scheme in the horizontal to solve the equations. The spatial scheme is upwind bias finite difference. The Arakawa C-grid discretisation is used spatially. Velocities are staggered at the edge of the cell [35]. Other variables such as geopotential, and potential temperature are staggered at the centre of the cell (also known as the mass point) [35].

The model uses terrain following hydrostatic pressure as the vertical coordinate [35]:

$$\eta = (p_{dh} - p_{dht})/\mu_d,$$

where $\mu_d = p_{hs} - p_{ht}$, p_{hs} is the dry hydrostatic surface pressure, p_{dh} is the dry hydrostatic pressure at a certain height, and p_{dht} is the dry hydrostatic pressure at the top of the domain. The moist momentum equations can be rewritten using the terrain-following vertical coordinate η. The other variables can also be adjusted using μ_d. $\mathbf{V} = \mu_d(u, v, w)$ is the covariant velocity, $\Theta = \mu_d\theta$ is the adjusted potential temperature, $\phi = gz$ is the geopotential, p is the pressure and $\alpha = 1/\rho$ is the specific volume. The divergence operator on a field is defined as

$$\nabla \cdot \mathbf{V}a = \frac{\partial(\mu_d u a)}{\partial x} + \frac{\partial(\mu_d v a)}{\partial y} + \frac{\partial\left(\mu_d \frac{d\eta}{dt} a\right)}{\partial \eta}$$

With all the definitions above, the moist equations of motion can be rewritten as [35]

$$\frac{\partial U}{\partial t} + (\nabla \cdot \mathbf{V}u) + \mu_d \alpha \frac{\partial p}{\partial x} + (\alpha/\alpha_d)\frac{\partial \phi}{\partial x}\frac{\partial p}{\partial \eta} = F_U, \tag{2.1a}$$

$$\frac{\partial V}{\partial t} + (\nabla \cdot \mathbf{V}v) + \mu_d \alpha \frac{\partial p}{\partial y} + (\alpha/\alpha_d)\frac{\partial \phi}{\partial y}\frac{\partial p}{\partial \eta} = F_V, \tag{2.1b}$$

$$\frac{\partial W}{\partial t} + (\nabla \cdot \mathbf{V}w) - g\left((\alpha/\alpha_d)\frac{\partial p}{\partial \eta} - \mu_d\right) = F_W, \tag{2.1c}$$

$$\frac{\partial \Theta}{\partial t} + (\nabla \cdot \mathbf{V}\theta) = F_\theta, \tag{2.1d}$$

$$\frac{\partial \mu_d}{\partial t} + (\nabla \cdot \mathbf{V}) = 0, \tag{2.1e}$$

$$\frac{\partial \phi}{\partial t} + \mu_d^{-1}[(\mathbf{V} \cdot \nabla\phi) - gW] = 0, \tag{2.1f}$$

$$\frac{\partial Q_m}{\partial t} + (\nabla \cdot \mathbf{V}q_m) = F_{Q_m}, \tag{2.1g}$$

$$\frac{\partial \phi}{\partial \eta} = -\alpha_d/\mu_d, \tag{2.1h}$$

$$p = p_0(R_d\theta_m/p_0\alpha_d)^\gamma, \tag{2.1i}$$

where the F_* terms on the right are forcing term from physics parameterisations, $\alpha = \alpha_d(1+q_v+q_c+q_r+q_i+...)^{-1}$ is the specific volume for the air parcel, and q_* are the mixing ratios for water vapour, cloud, rain, ice etc. Also, $\theta_m = \theta(1 + (R_v/R_d)q_d) \approx \theta(1 + 1.61q_v)$ and $Q_* = \mu_d q_*$.

2.2 Simulation Setup

The setup of the simulation is similar to the setup in Bryan and Morrison [8] except for the initial temperature and moisture profiles. Simulations are performed with WRF. The domain size is 576 km in the streamwise (x) direction, 144 km in the spanwise (y) direction, and 25 km in the vertical. In all simulations, the vertical grid is fixed with 100 grid levels with non-uniform grid spacings from 220 m at the bottom to 900 m at the top of the domain. The vertical resolution is higher near the surface to resolve boundary layer turbulence. The horizontal resolutions are $\Delta x = \Delta y = 4$ km, 1 km, 500 m and 250 m. All 12 squall line simulations presented in this thesis are run for 6 hours. A time step of 3 seconds is used for the 4 km, 1 km and 500 m simulations, and 1 second is used for the 250 m simulation. Three subgrid turbulence schemes are used in this project: the prognostic TKE closure, the 3D Smagorinsky closure and the no subgrid turbulence scheme.

The Weisman and Klemp [44] sounding profile is used in this project. This is the same sounding shown in Fig. 1.1. The profile has low level wind shear in x with wind speeds varying from 11 ms^{-1} to 0 ms^{-1} over a height of 2.5 km is used. The model is further initialized with a cold pool as in Weisman et al. [45]. The cold pool is a 2 km deep region on the west half of the domain, with a potential temperature perturbation of -8 K set on the surface, which increases linearly to 0 K at 2 km above the surface. Random temperature perturbations of 0.008 K are added to the lowest grid level. Open boundary conditions are used in the x direction, and periodic boundary conditions are used in the y direction. The initial potential temperature and water vapour mixing ratio field are shown in Fig. 2.1.

The microphysics scheme used in this project is the Lin et al. [24] single moment scheme, which is a single moment microphysics scheme with graupel included. It includes six species of water: vapour, liquid cloud water, ice cloud water, rain water, snow, and graupel. The drag coefficient is set to be 0.01. Radiative cooling is turned off. For the surface layer option, the Revised MM5 scheme [16] is used. Surface heat and moisture fluxed are not included. Rayleigh damping is used in the top 5 km of the domain (from 20-25 km, not shown in the following figures) with a damping coefficient set to 0.003.

2.3 Diagnostics

The speed of the squall line is determined by tracking the x position of the point with the maximum vertical velocity over the whole domain. The mean propagation speed is calculated for the mature squall line from 200 minutes to 350 minutes.

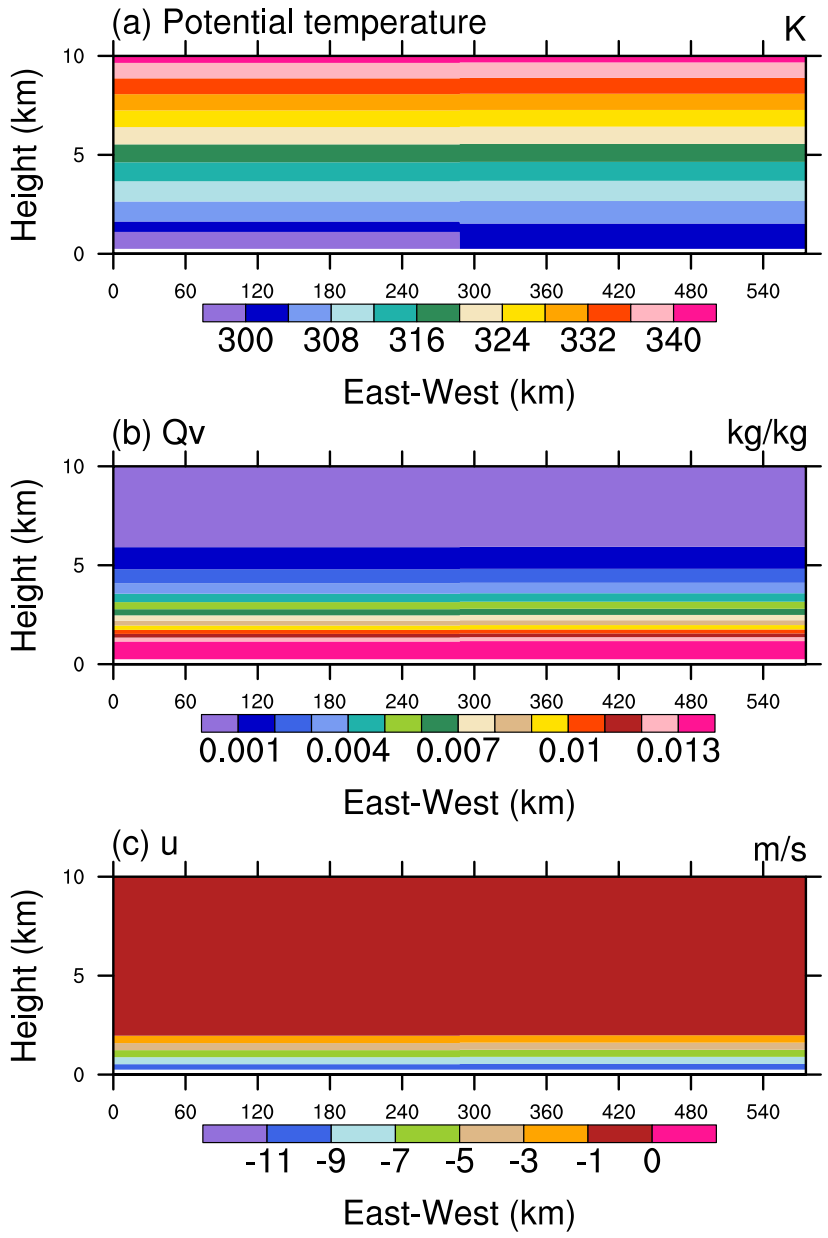

Figure 2.1: Initial profile for the simulation: Figure (a) is a vertical slice of the initial potential temperature. The purple region on the bottom left is the cold pool. Figure (b) is a vertical slice of the initial water vapour mixing ratio profile. Figure (c) is a vertical slice of the initial velocity (u) in the East-West (x-) direction.

Simulations	Δx	Δt	Mixing Scheme
TKE250	250 m	1 s	TKE
TKE500	500 m	3 s	TKE
TKE1000	1 km	3 s	TKE
TKE4000	4 km	3 s	TKE
SMA250	250 m	1 s	Smagorinsky
SMA500	500 m	3 s	Smagorinsky
SMA1000	1 km	3 s	Smagorinsky
SMA4000	4 km	3 s	Smagorinsky
NoMix250	250 m	1 s	No Mixing
NoMix500	500 m	3 s	No Mixing
NoMix1000	1 km	3 s	No Mixing
NoMix4000	4 km	3 s	No Mixing

Table 2.1: List of simulations.

The mass flux is calculated by the domain sum of $\rho \max(w,0)\Delta x \Delta y$ [8]. Cloud top height is calculated by finding the height of the highest point with the horizontal averaged cloud water mixing ratio less than 0.001 g/kg.

The energy spectra are calculated following [9]. At height $z = 5$ km, the y-average vertical velocity is computed, and the point with the maximum fluctuation of w from the y-average is computed. A one-dimensional y-spectrum is computed of w through this point.

The subgrid TKE ratio R is calculated similarly to Bryan et al. [9] as

$$R(x,z) = \frac{\langle e \rangle}{\langle e + E \rangle} \tag{2.2}$$

where e is the subgrid TKE from the LES scheme, the resolved TKE is defined as

$$E(x,y,z) = \frac{1}{2}\left((u - \langle u \rangle)^2 + (v - \langle v \rangle)^2 + (w - \langle w \rangle)^2\right)$$

and the $\langle . \rangle$ represent the spanwise average.

2.3.1 Subfilter Energy Transfer

High-resolution LES can be filtered to analyze energy transfers across different length scales. The equation for the filtered kinetic energy $q = \overline{u}_i \overline{u}_i / 2$ can be obtained by mul-

tiplying (1.34) by $\overline{u}_i$ and simplifying. We use the anelastic continuity equation (1.32) to simplify. The resulting equation is:

$$\widetilde{\rho}\frac{\partial q}{\partial t} + \frac{(\widetilde{\rho}\,\overline{u_i}q)}{\partial x_i} + \frac{\partial(\widetilde{\rho}\,\overline{u_i}\widetilde{\tau_{ij}})}{\partial x_j} + -\frac{1}{\widetilde{\rho}}\frac{\partial(\widetilde{\rho}u_i p)}{\partial x_i} = \widetilde{\rho}\,\widetilde{\tau_{ij}}\overline{s_{ij}}. \tag{2.3}$$

On the right side of the equation, the term $\widetilde{\rho}\,\widetilde{\tau_{ij}}\overline{s_{ij}}$ is the transfer of kinetic energy from filtered to subfilter scales. For eddy viscosity, it is a sink term, also known as turbulence dissipation. However, in general, it can locally be a source term, which is called backscatter (e.g. [30]).

The subfilter energy transfer rate P is defined following Piomelli et al. [29] as

$$P = \iiint \widetilde{\rho}\,\widetilde{\tau_{ij}}\overline{s_{ij}}dxdydz. \tag{2.4}$$

Furthermore, P can be separated into negative (dissipation) and positive (backscatter) contributions, where the dissipation ϵ_- and the backscatter ϵ_+ are defined as [29]

$$\epsilon_+ = \frac{1}{2}\left(P + |P|\right),$$

$$\epsilon_- = \frac{1}{2}\left(P - |P|\right).$$

The backscatter represent energy transfer from subfilter to filtered scales, and is neglected in eddy viscosity LES models. In this thesis, we compute P with a horizontal box-filter

$$\overline{u(a,b)} = \frac{1}{\Delta^2}\int_{a-\frac{\Delta}{2}}^{a+\frac{\Delta}{2}}\int_{b-\frac{\Delta}{2}}^{b+\frac{\Delta}{2}} u(x,y)dxdy,$$

where the integral is computed with the trapezoidal scheme. Since filtered fields are computed to investigate the dynamics of different grid spacings, and only horizontal resolution is varied, we do not filter fields in the vertical.

Also note that the full vertical domain of the x-z plots presented in this projects is not shown, because the cloud top is about 10 km. For clarity, only the troposphere up to 10 km, rather than the full model domain up to 25 km, is shown. The full domain height is 25 km and the Rayleigh damping is used in the top 5 km of the domain.

Results are presented in the next chapter. The main focus is on the TKE simulations, and some discussion on the Smagorinsky scheme is placed at the end of the section. Conclusions and an outline of future work are given in chapter 4.

Chapter 3

Results

3.1 Structure

In this section, the structure of the simulated squall line with $\Delta x = 250$ m and the TKE mixing scheme will be discussed. This simulation is the best resolved case and will be compared to the other cases in this project. The squall line has a main updraft at the leading (right) side and clouds are trailing behind the main updraft. The cloud top height is approximately 9 km. The propagation speed of the squall line is approximately 11.6 ms^{-1}. The potential temperature and the cloud water mixing ratio will be used for discussions in this section. Figure 3.1 shows the total mass flux (computed following Bryan and Morrison [8]) and the precipitation rate of the storm with time. As shown from the plot, the squall line takes about 90 minutes to become fully developed with maximum mass flux and precipitation; after this time, both quantities decrease slowly.

Figure 3.2 shows the spanwise averaged cloud water mixing ratio at 30 minutes, 90 minutes, 120 minutes, 180 minutes, 240 minutes and 300 minutes. From Fig. 3.2, one can see the classic structure of a trailing stratiform squall line with upshear (reward) tilt (e.g. [23]). The squall line starts as a convective plume response to the initial perturbation in the first 60 minutes. There is not much cloud trailing behind the main updraft before the storm becomes mature. At 90 minutes, discrete and individual structures start to form behind the main updraft. At 120 minutes, the trailing clouds are attached to each other closely. At this stage, the amount of cloud water in the main updraft starts to decrease as the storm propagates. At 180 minutes, the cloud water mixing ratio of the main core reduces significantly. At 240 minutes, as the storm propagates, the amount of trailing cloud increases, creating a tail of trailing clouds behind the main updraft. In addition, a

small region of cloud forms ahead of the squall line. At 240 minutes, the storm interacts with the east boundary and creates a new structure ahead of the main storm.

Figure 3.3 shows horizontal cross sections of potential temperature at height of 2 km at the same times as in Fig. 3.2. Spanwise averaged w rather than w^2 is shown to illustrate the structure of the large scale updraft. Before 50 minutes, the storm is essentially two-dimensional, with a very straight line structure from north to south. At 90 minutes, more random structures in y are developing. At 120 minutes, the storm is fully three-dimensionalised and non-uniform from north to south. The fully developed storm has a warm leading edge, associated with latent heating at this height, with a colder irregular trailing structure due to the evaporation of rain. The front edge starts wobbling at about 180 minutes. The wobbling leading edge can also be seen at 240 minutes. When wobbling starts to happen, mixing inside the warm leading edge can also be seen. As the leading warm region become turbulent, the trailing cold region also becomes warmer. As a result, the wobbling is related to the three-dimensionalisation of the storm.

Figure 3.4 shows the evolution of the spanwise averaged vertical velocity at the same time as above. At earlier stages of the mature storm ($t = 90$ minutes), the storm is dominated by a strong updraft with the average vertical velocity of around 10 ms^{-1}. Downdrafts and smaller magnitude structures can also be found (e.g. near $x = 280$ km at $t = 90$ minutes). At 180 minutes, the storm is dominated by the updraft with a weaker downdraft behind. The tilted form of the squall line can be seen clearly at this time. At later times, the storm updraft is weakened and the size of the updraft becomes smaller.

3.2 Sensitivity to Resolution

In this section, the sensitivity of the simulated squall line to grid resolution will be discussed. The TKE scheme simulations will be used; the sensitivity to mixing scheme will be considered in the next section. The spanwise (y) averaged cloud water mixing ratio and vertical velocity, horizontal slices of potential temperature, and time series of mass flux and precipitation rate will be used for comparison.

Figures 3.5 and 3.6 show the spanwise averaged cloud water mixing ratio at different resolutions at time 120 minutes and 240 minutes. The lowest horizontal resolution of 4 km is able to produce the general structure of the squall line with the tilting and trailing stratiform clouds. However, the $\Delta x = 4$ km case can only produce a large convective plume with a large trailing cloud, without resolving the details of the convective structure in the squall line. The effect on the cloud water mixing ratio field is significant when the resolution

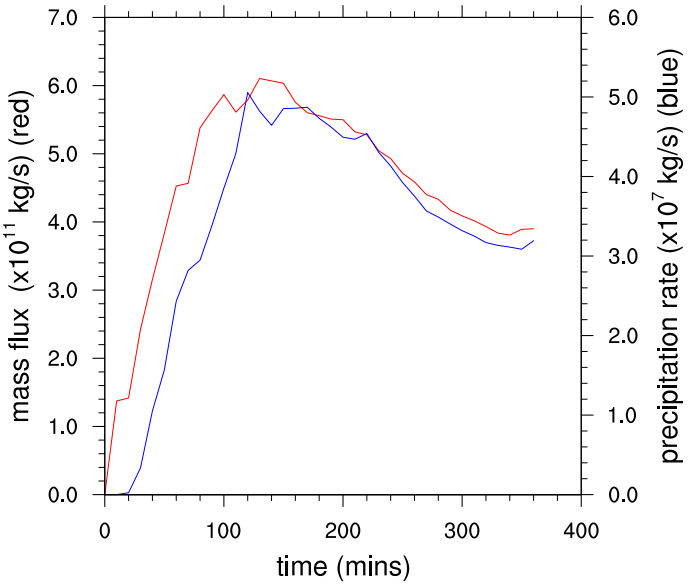

Figure 3.1: Mass flux (red) and precipitation rate (blue) with time from the TKE simulation with $\Delta x = 250$ m.

increases from $\Delta x = 4$ km to 1 km. The simulation with $\Delta x = 1$ km shows more details and discrete structures. The $\Delta x = 1$ km simulation also produces banded structures in the trailing clouds that do not appear at either lower or higher resolution. As the resolution increases further, the size of the trailing stratiform region decreases, suggesting that the 1 km and 4 km simulations have unrealistically long trailing structures. These results suggest that TKE mixing scheme has difficulties in correctly modelling subgrid mixing at a resolution of 1 km.

The simulation with $\Delta x = 500$ m has a smaller stratiform region than the lower resolution simulations, and the peculiar banded structures found with the $\Delta x = 1$ km simulation is absent. The $\Delta x = 500$ m simulation has the most cloud water concentrated in the main updraft core and larger cloud heights than for the $\Delta x = 1$ km simulation. Such effects may be due to the insufficient mixing in the main updraft area. The further increase of the resolution from $\Delta x = 500$ m to 250 m certainly has a significant effect on the structure of the storm. Less cloud water at the main updraft core and larger trailing cloud occur in the $\Delta x = 250$ m case.

In general, squall lines simulated at higher resolution show more detailed structures. Also, lower resolution case yields a larger and more attached structure, while a higher resolution case gives a smaller and more separated structure. The dependence of the individual cell

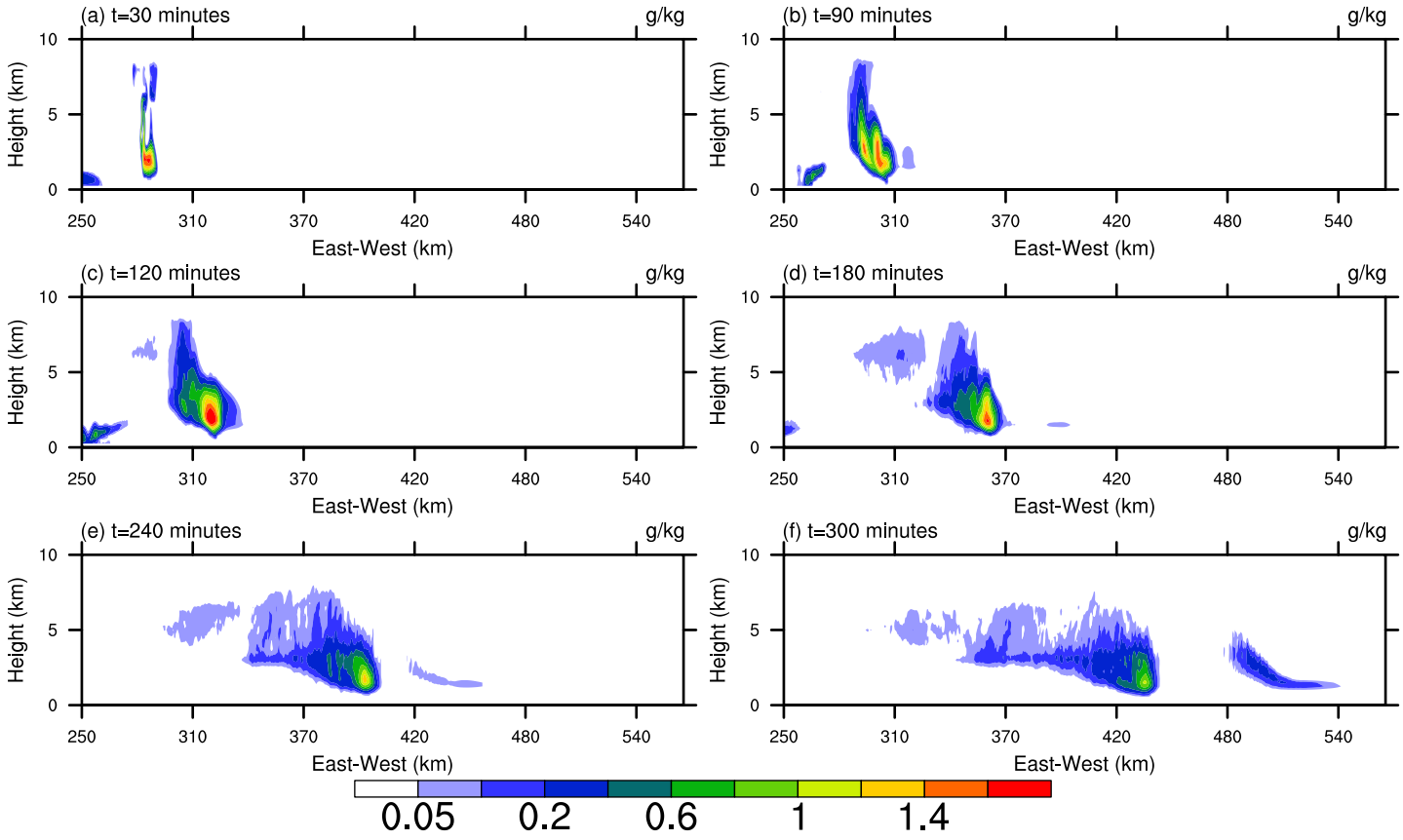

Figure 3.2: Spanwise (y) averaged cloud water mixing ratio for the TKE simulation with $\Delta x = 250$ m at (a) 30 minutes, (b) 90 minutes, (c) 120 minutes, (d) 180 minutes, (e) 240 minutes, and (f) 300 minutes. For clarity, only the right half of the domain is shown.

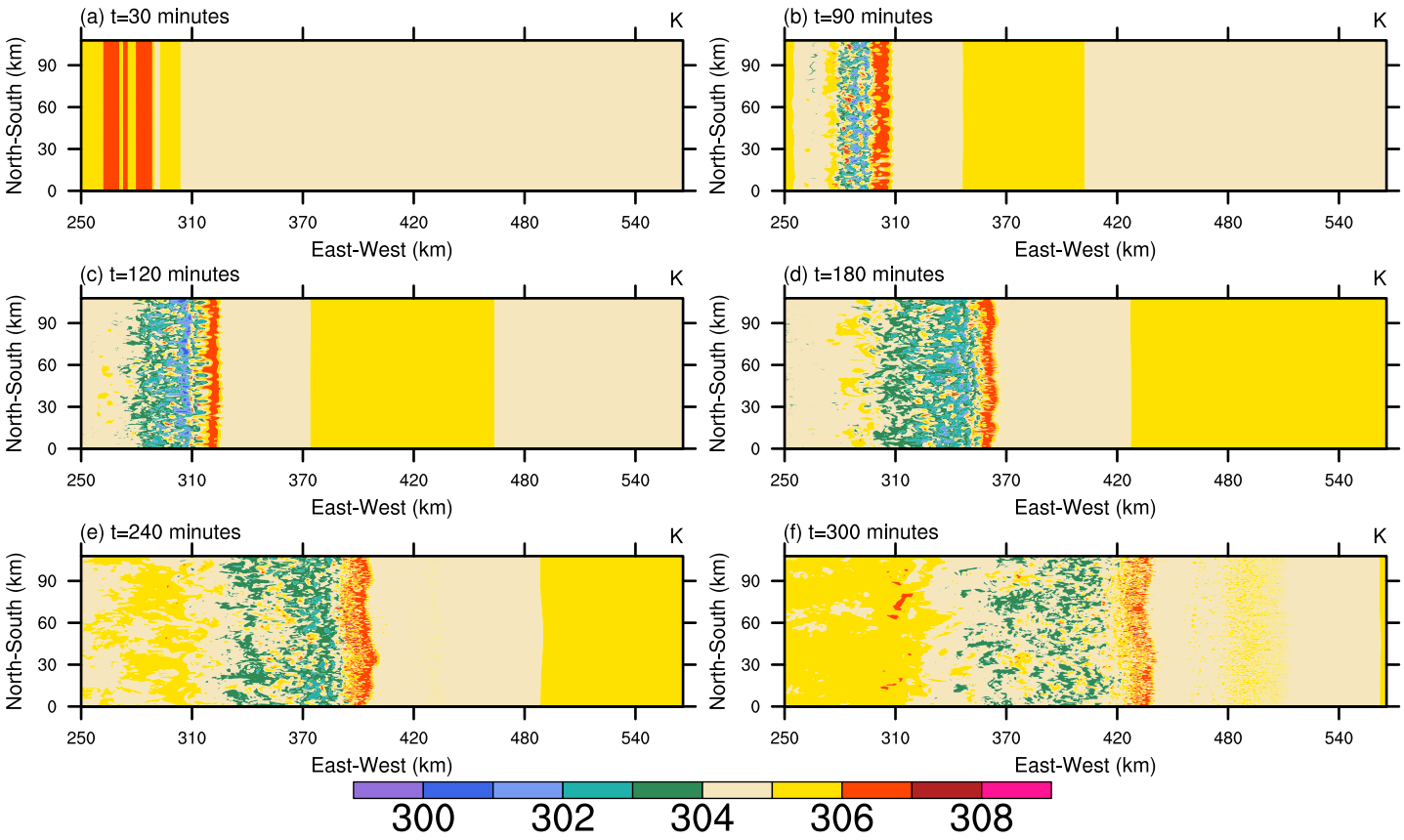

Figure 3.3: Horizontal slices of potential temperature at height of 2 km for the TKE simulation with $\Delta x = 250$ m at (a) 30 minutes, (b) 90 minutes, (c) 120 minutes, (d) 180 minutes, (e) 240 minutes, and (f) 300 minutes. For clarity, only the right half of the domain is shown.

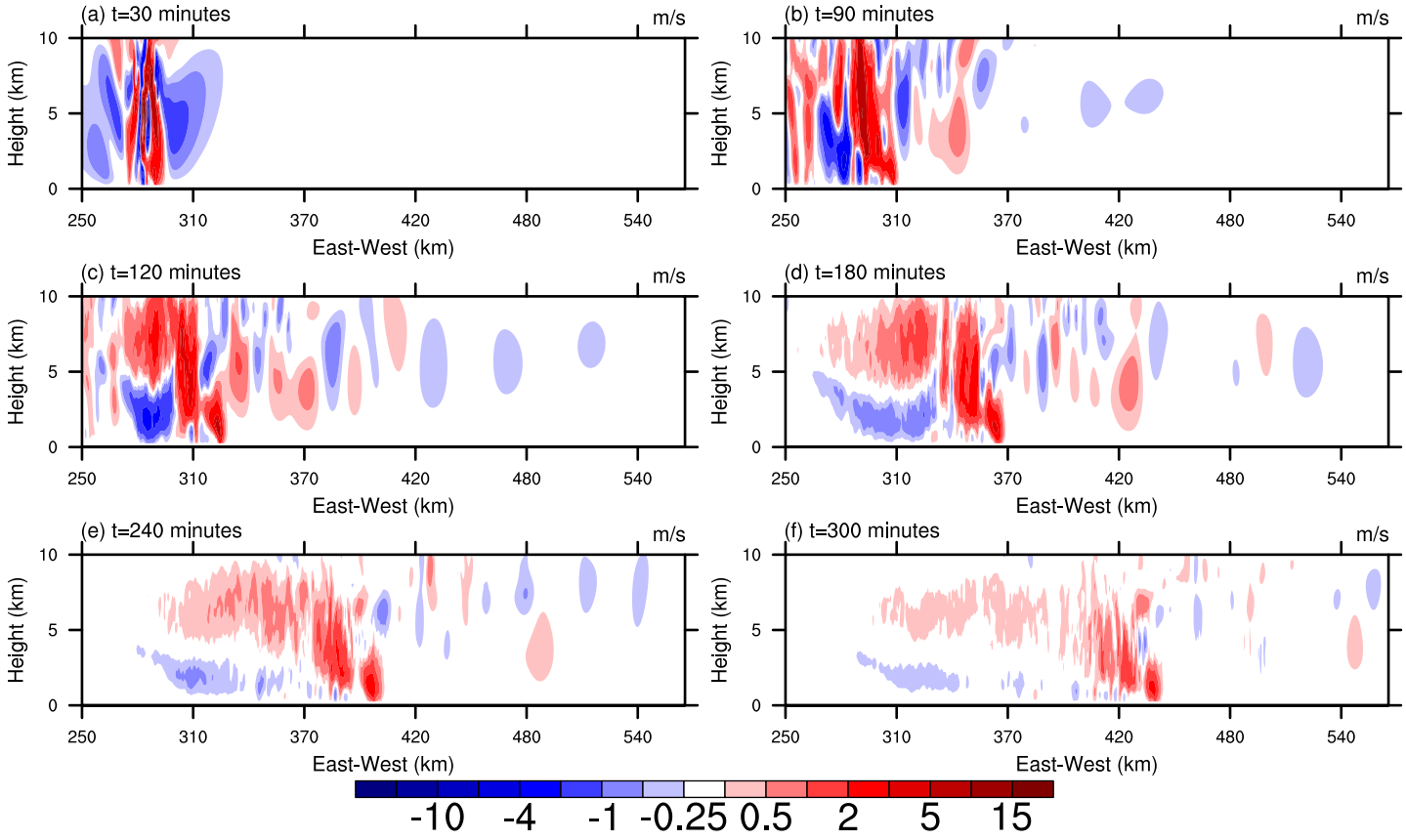

Figure 3.4: Spanwise (y) averaged vertical velocity for the TKE simulation with $\Delta x = 250$ m at (a) 30 minutes, (b) 90 minutes, (c) 120 minutes, (d) 180 minutes, (e) 240 minutes, and (f) 300 minutes. For clarity, only the right half of the domain is shown.

size on resolution is also been suggested by some studies such as Bryan and Morrison [8] and Bryan et al. [9].

Cloud top height is a common measurement of the intensity of a squall line. Overall, the cloud top heights are similar at different resolutions and there is no significant trend with the increase of the resolution. The $\Delta x = 4$ km simulations have the lowest cloud top, but the change with the increasing resolution is not significant. For example, the cloud heights in Fig. 3.6 are 8 km, 7 km, 8 km, and 7 km for $\Delta x = 4$ km, 1 km, 500 m, and 250 m. This finding is in contrast to past studies that have found a more significant impact of the resolution on cloud depth ([42]), and Bryan and Morrison [8] found the highest cloud top with $\Delta x = 1$ km.

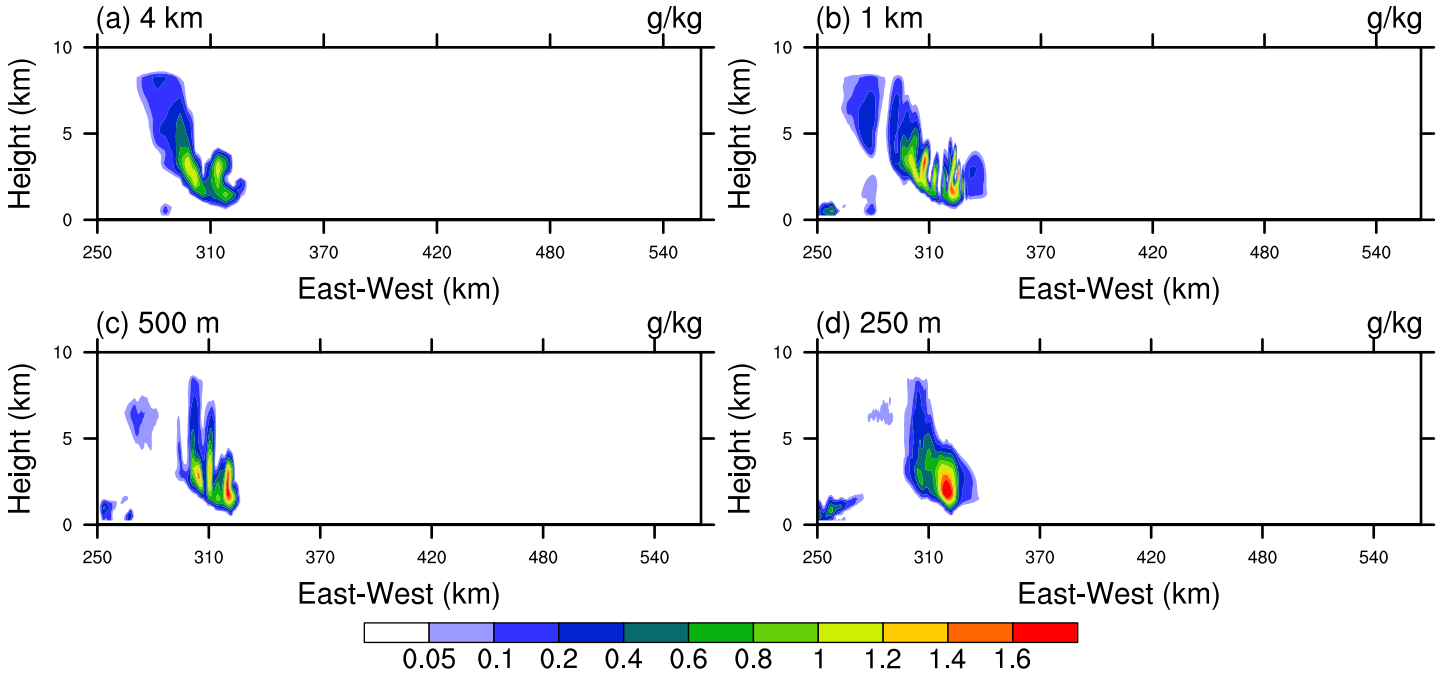

Figure 3.5: Spanwise (y) averaged cloud water mixing ratio for the TKE simulation with resolutions $\Delta x =$ (a) 4 km, (b) 1 km, (c) 500 m, and (d) 250 m at 120 minutes. For clarity, only the right half of the domain is shown.

The spanwise averaged vertical velocity (Fig. 3.7) characterizes the intensity of the convection. The size and number of individual updraft cores are sensitive to the resolution. Lower resolution results in one large updraft core, while high resolution gives more individual and smaller updraft structures. The dependence of the updraft core area on the

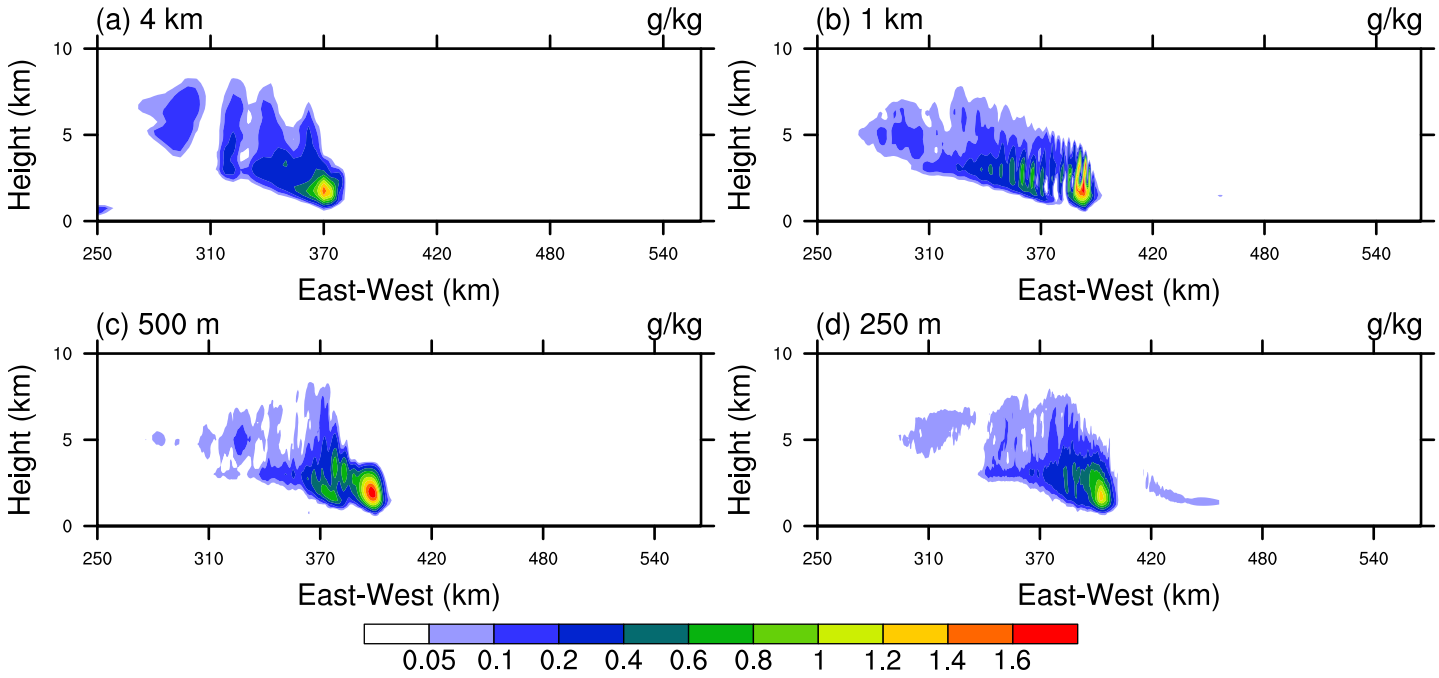

Figure 3.6: Spanwise (y) averaged cloud water mixing ratio for the TKE simulation with resolutions Δx = (a) 4 km, (b) 1 km, (c) 500 m, and (d) 250 m at 240 minutes. For clarity, only the right half of the domain is shown.

resolution has also been shown by Lebo and Morrison [20]. From Table 3.1, the maximum vertical velocity approaches 60 ms^{-1} as resolution increases to $\Delta x = 250$ m.

The propagation speeds of the higher resolution cases are slightly faster than the lower resolution cases: for the TKE scheme, the speed increases from 8.9 ms^{-1} at $\Delta x = 4$ km to 11.6 ms^{-1} for $\Delta x = 250$ m.

The potential temperature can also be useful in understanding the effect of the resolution on the storm structure. The horizontal slices of potential temperature at a height of 2 km at different resolutions are shown in Fig. 3.8. All 4 resolutions have a warm leading edge and a cold turbulent region trailing behind. Different features can be seen at different resolutions. At $\Delta x = 4$ km, the front is straight with almost no variation in y. There is no small scale structure in the trailing cold turbulent region for $\Delta x = 4$ km. The $\Delta x = 1$ km case shows more turbulent mixing of the potential temperature in both the leading front and the trailing cold region, e.g. the banded structure behind the leading edge, which is not shown by the simulation with $\Delta x = 4$ km. The banded structures appear to be

Resolution	TKE	SMA	NoMix
(a) Mean propagation speed (ms^{-1})			
4 km	8.9	2.7	6.7
1 km	10.0	7.9	8.2
500 m	11.0	10.2	7.8
250 m	11.6	10.2	8.0
(b) Maximum vertical velocity (ms^{-1})			
4 km	20.2	26.0	28.8
1 km	29.4	39.8	44.9
500 m	48.6	48.6	60.9
250 m	60.1	62.2	64.9
(c) Maximum precipitation rate (x10^7 kg/s)			
4 km	4.78	4.31	5.38
1 km	4.91	5.67	5.16
500 m	4.80	5.49	4.92
250 m	5.06	4.76	4.79
(d) Maximum mass flux (x10^{11} kg/s)			
4 km	5.17	4.59	5.17
1 km	6.74	6.90	6.74
500 m	7.53	7.12	7.53
250 m	6.10	6.01	6.10
(e) Cloud top height (km)			
4 km	9.849	10.02	10.00
1 km	9.996	10.05	10.00
500 m	10.01	10.02	10.23
250 m	10.02	10.01	10.02

Table 3.1: (a) Mean propagation speed, (b) maximum vertical velocity, (c) maximum precipitation rate, (d) maximum mass flux, and (e) maximum cloud top height.

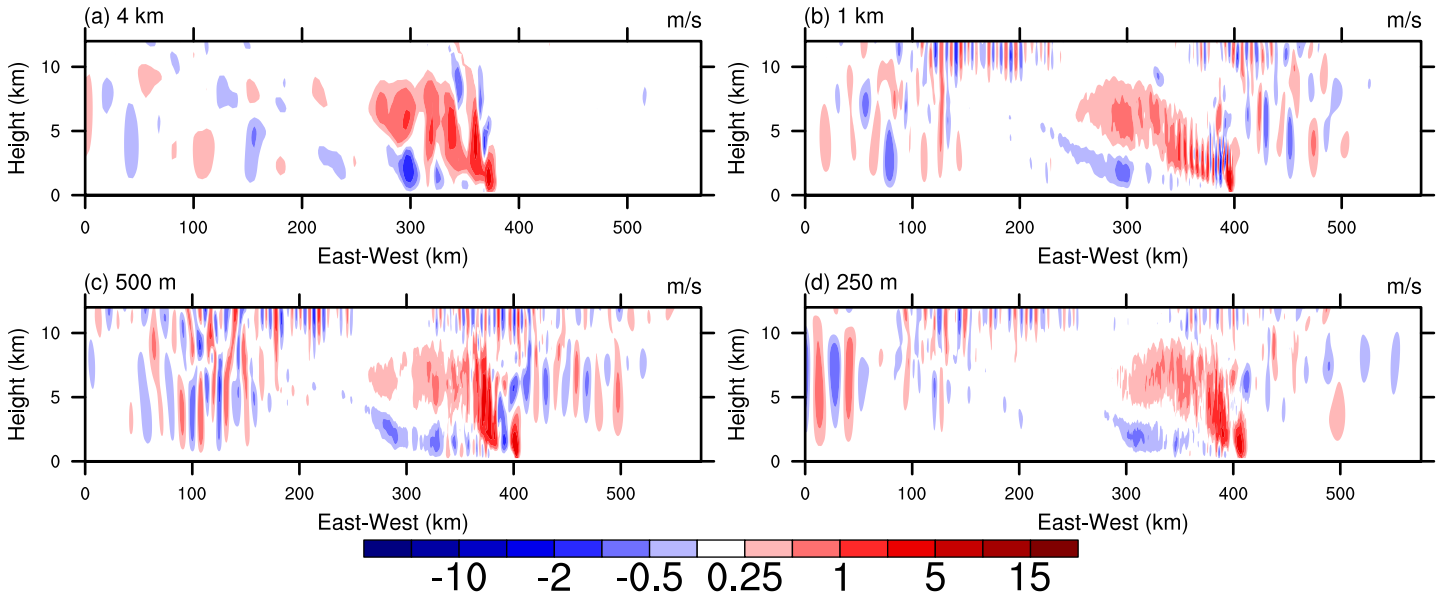

Figure 3.7: Spanwise (y) averaged vertical velocity for the TKE simulation with resolutions Δx = (a) 4 km, (b) 1 km, (c) 500 m, and (d) 250 m at 240 minutes.

related to the three-dimensionalisation, and they become turbulent later in the simulation. In cases with grid spacing smaller than 500 m, such line structures do not exist after the storm is fully developed.

Also, the wobbling of the leading front edge can be observed with grid spacing smaller than $\Delta x = 1$ km. At $\Delta x = 500$ m, a solid thick warm front can be seen, which is not seen with higher resolution $\Delta x = 250$ m. The area of the solid warm front with $\Delta x = 500$ m is similar to the area of the line structure with $\Delta x = 1$ km. More details on the structure can be seen in the $\Delta x = 500$ m case than the 1 km case at earlier times. A similar mixing pattern can be seen in both high resolution simulations, which produce more small scale eddies. The amount of wobbling at the leading edge of the $\Delta x = 500$ m case is similar to that in the $\Delta x = 1$ km case. The area of the warm leading edge of the $\Delta x = 250$ m case is shorter than the warm leading edge of the $\Delta x = 500$ m throughout the 6 hours simulation. The warm leading front of the $\Delta x = 250$ case is slightly colder than the leading front in the $\Delta x = 500$ m case. The cold region of both the $\Delta x = 500$ m and 250 m case are similar. Overall, the lower resolution simulations also take a longer time to three-diimensionalised. The leading edge of the squall line in the higher resolution simulation has more wobbling. The wobbling is believed to be related to instability and three-dimensionalisation of the turbulent in the warm leading front. Such wobbling of the leading edge can also be found

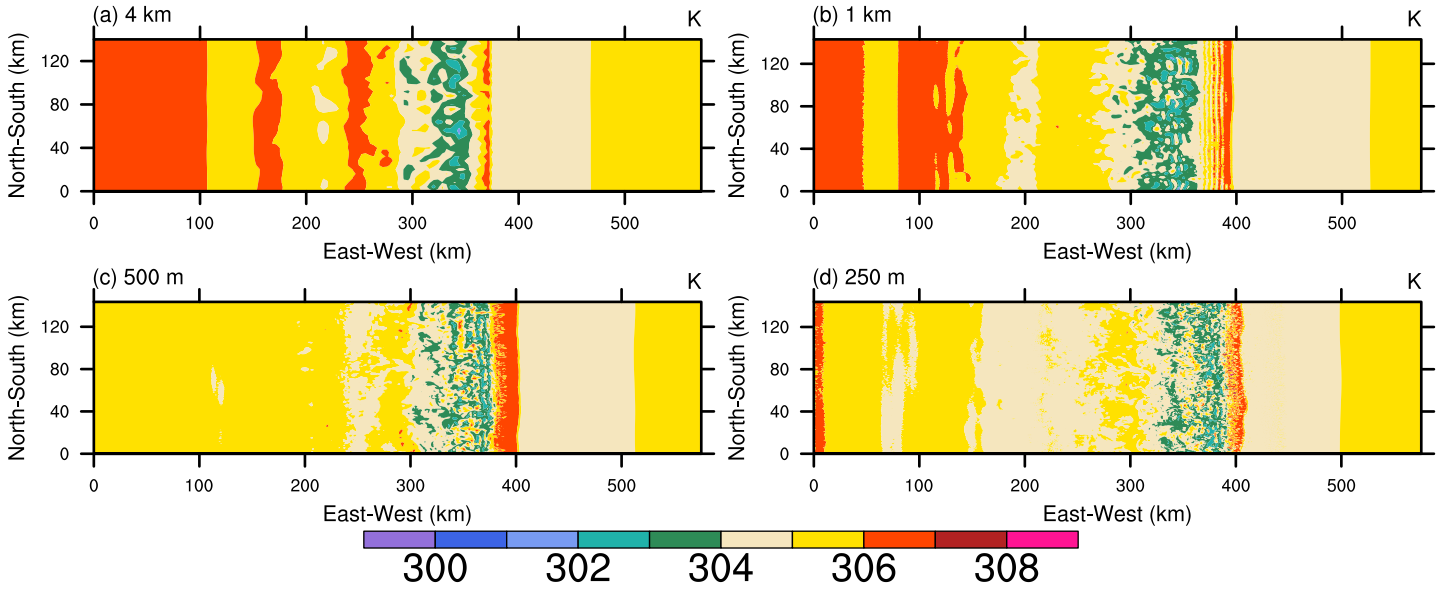

Figure 3.8: Horizontal slice of potential temperature at height of 2 km for the TKE simulation with resolutions Δx = (a) 4 km, (b) 1 km, (c) 500 m, and (d) 250 m at 240 minutes.

in Bryan et al. [9].

Figure 3.9(a) shows time series of mass flux for the TKE simulations at different resolutions. A clear rank can be given according to the magnitude of the mass flux after the squall line mature: In ascending order: $\Delta x = 4$ km, 250 m, 1 km and 500 m. The large jump in mass flux as grid spacing changes from $\Delta x = 4$ km to 1 km is likely due to the effect of increased resolution on nonhydrostatic processes as suggested by Weisman et al. [45]. As the resolution increases from $\Delta x = 1$ km to 500 m, the mass flux continues to increase significantly. As the grid is further refined to $\Delta x = 250$ m, the mass flux drops by about 20 percent. This nonmonotonic behaviour is likely due to the competition between resolved and unresolved processes.

Consider Fig. 3.9(d) shows the time series of the precipitation rate for the TKE simulations at different resolutions. In general, no clear trend can be identified as the resolution increases. Nevertheless, some interesting dependence of precipitation rate on Δx can be seen. For example, the time at which the precipitation peaks is different. The precipitation rate peaks earlier (around 80 minutes) in the $\Delta x = 1$ km case than in the other cases (around 100 to 120 minutes). Moreover, the precipitation rates decrease after 200 minutes in all cases. The maximum values of the precipitation rates are similar in all cases and do

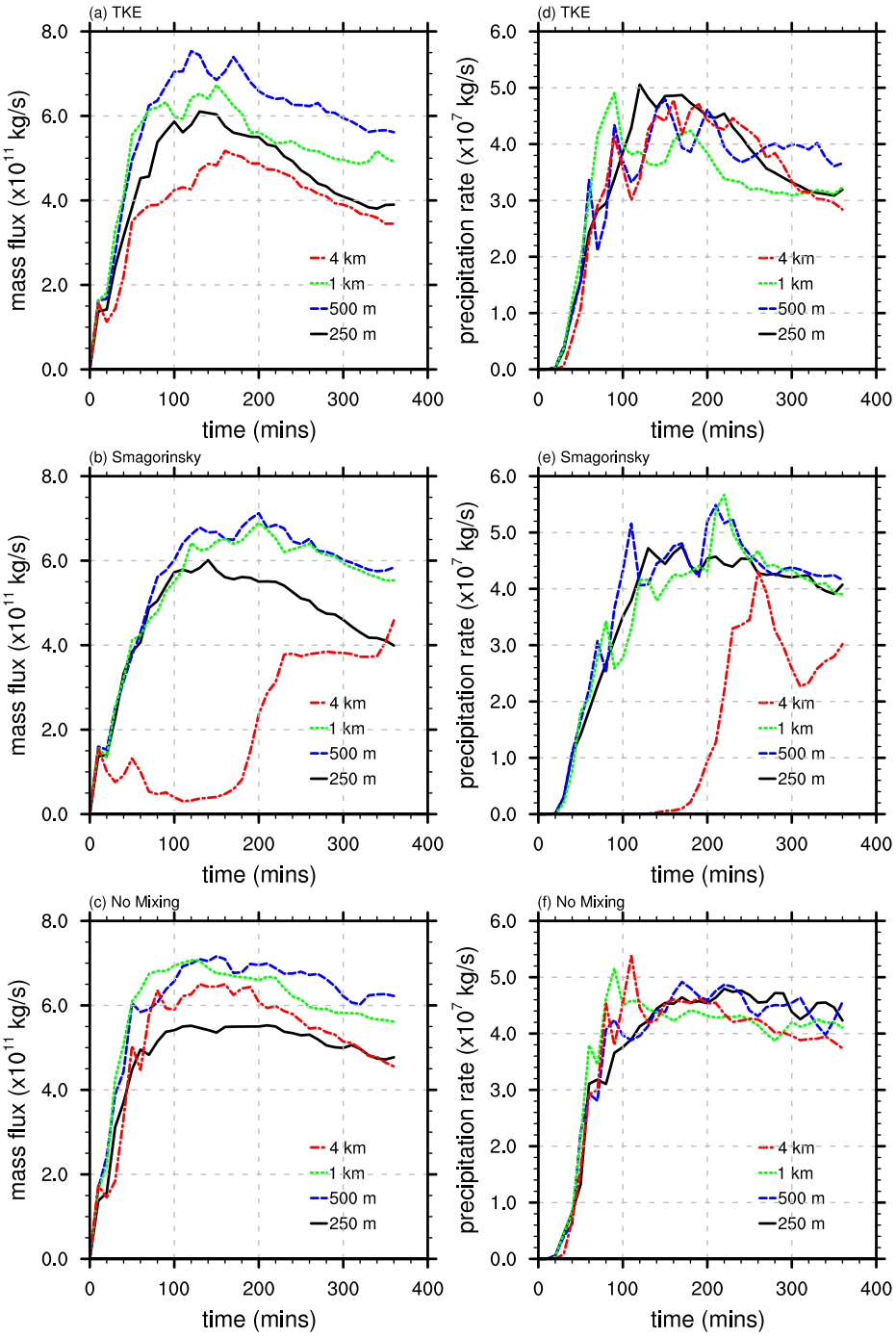

Figure 3.9: Time series of mass flux for simulations with (a) TKE, (b) Smagorinsky, and (c) no mixing. Time series of precipitation rate for simulations with (d) TKE, (e) Smagorinsky, and (f) no mixing.

not depend much on Δx. The $\Delta x = 250$ m case has the highest precipitation rate by a small margin. The dependence of precipitation rate on the resolution is found in different studies. Bryan and Morrison [8] suggests that increased resolution results in decreased precipitation.

The vertical velocity kinetic energy spectra in y are plotted in Fig. 3.10. The method for obtaining the spectra is described in section 2.3. While the spectra are very noisy, the high resolution simulations show a broad maximum around $k = 70$, corresponding to a wavelength of around 2 km. These are the scales of the most energetic convective plumes. The resolution of $\Delta x = 4$ km is not sufficient for resolving these scales, and $\Delta x = 1$ km only marginally resolves them.

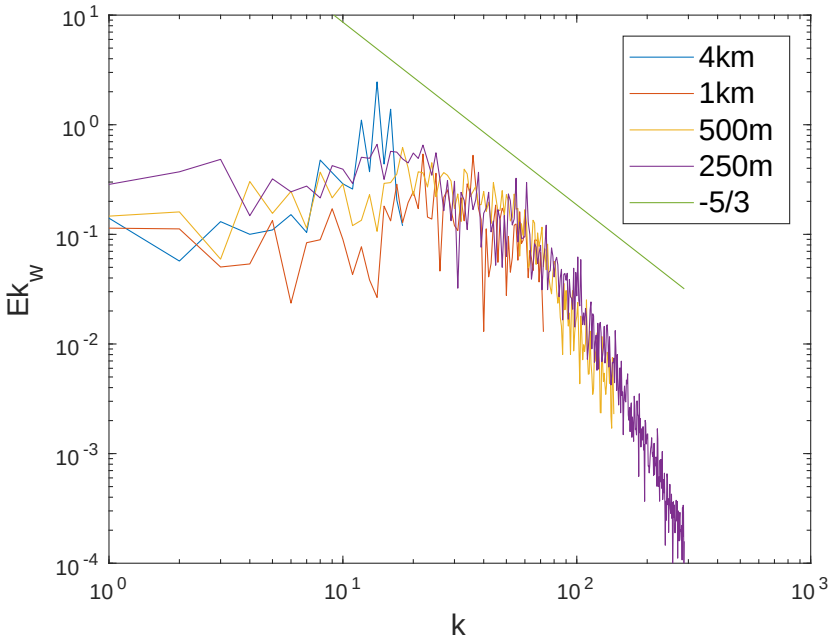

Figure 3.10: One dimensional (spanwise) vertical velocity kinetic energy spectrum at height of 5 km and x of maximum variance [9] for TKE at resolutions 4 km, 1 km, 500 m, and 250 m. Wavenumbers are nondimensional, so $k = 1$ corresponds to the wavelength of the spanwise domain size 144 km. The green line has a slope of -5/3. At the end of the result section, the energy spectra for Smagorinsky simulations (Fig. 3.21) are also presented for comparison.

3.3 Sensitivity to Scheme

The above section focused on the dependence of the squall line simulations on resolution when the TKE scheme is used. In this section, we consider the dependence on subgrid mixing scheme. Additional simulations with Smagorinsky mixing and with no subgrid scheme are performed at all resolutions.

Overall, at a fixed resolution, the squall line is sensitive to the subgrid mixing scheme. Simulations with different schemes (Fig. 3.6, Fig. 3.11 and Fig. 3.12) are able to produce a trailing stratiform squall line within the 6 hours simulation time. From the mass flux (Fig. 3.9a-c) and precipitation rate (Fig. 3.9d-f), one can see that the squall line in the simulation with $\Delta x = 4$ km and the Smagorinsky scheme is significantly delayed. The Smagorinsky simulation with $\Delta x = 4$ km is not able to generate sufficient convection to initiate the squall line during the first half of the simulation time. Simulations with TKE and no mixing scheme are able to create a propagating squall line at the lowest resolutions, although the speed is slightly slower than in the higher resolution simulations.

Figures 3.11 and 3.12 show the spanwise averaged cloud water mixing ratio at 240 minutes for the simulations with the Smagorinsky mixing and no mixing, respectively, at all resolutions. These can be compared to Fig. 3.6 for the corresponding results with the TKE mixing at 240 minutes. Simulations with the Smagorinsky scheme simulations can only produce the correct shape of the squall line when $\Delta x \leq 1$ km. Note that the resolution of $\Delta x = 4$ km inhibits the squall line with Smagorinsky mixing, while such an effect is not seen in the TKE or no subgrid mixing simulations. This shows that Smagorinsky mixing should not be used with $\Delta x = 4$ km for simulations of convective systems with explicitly resolved convection. By contrast, simulations with the TKE scheme and no mixing scheme are able to produce the general shape of the squall line even at $\Delta x = 4$ km.

At a fixed resolution, the Smagorinsky mixing simulations have more cloud water in the trailing region behind the main core compared to other mixing schemes and have significantly less cloud water in the main core compared to the no subgrid mixing simulations. These differences in the core cloud water are due to the fact that Smagorinsky mixing is very diffusive, while no subgrid mixing prevents the core cloud water from mixing with the surrounding regions. At a later time (6 hours, not shown), while the long trailing structure can be found the TKE mixing scheme simulations at all resolutions, this structure is not seen in the other simulations.

Consider the horizontal slice of potential temperature at height 2 km for the Smagorinsky mixing scheme at 240 minutes, shown in Fig. 3.14. While the warm leading region exists, the region is not turbulent even at the high resolution. Such a result can also be seen in

Fig. 3.11. This finding may explain the fact that at the same resolution, the Smagorinsky mixing simulations are not showing the same level of detail in structures as the TKE mixing simulation does. With Smagorinsky mixing, the changes in details in structures are not as significant as the resolution increases.

Simulations with different mixing schemes have similar cloud top height of 10 km (table 3.1). Cloud top height is not significantly affected by the resolution and mixing scheme. Such results are interesting given the changes of cloud top height with resolutions found in Bryan and Morrison [8] and Waite and Khouider [42], which suggested that cloud height can sometimes depend on subgrid mixings. These results suggest that the dependence of the cloud top height on the resolution and subgrid mixing may occur when certain environmental conditions are present, such as the high CAPE environmental setting in Bryan and Morrison [8].

Figure 3.13 shows the spanwise averaged vertical velocity with the Smagorinsky mixing scheme at different resolutions at 240 minutes. At $\Delta x = 500$ m and 250 m, the overall shape of the averaged structure shown for the Smagorinsky mixing simulations are similar to the TKE mixing simulations from Fig. 3.7. The trailing updraft region in the Smagorinsky simulation is slightly smaller, and the main updraft core is slightly stronger than those with the TKE mixing schemes.

The maximum vertical velocity (table 3.1) in the storm with no subgrid mixing is the largest at a given resolution, and it increases with the resolution to a maximum of 65 ms^{-1} for $\Delta x = 250$ m. The propagation speed (table 3.1) also depends on the mixing scheme. At the same resolution, storms with TKE mixing propagate the fastest, the storms with Smagorinsky mixing propagates the second fastest, and those with no mixing propagates the slowest. With a fixed mixing scheme, the convergence of propagation speed as resolution increases can be seen. The significantly slower propagation speed of the storm with no mixing scheme may be due to the fact that the squall line in this case is not as titled as the squall line in simulations with other mixing schemes. The tilting will affect the circulation created by the downdraft due to precipitation, and hence modifies the propagation speed.

Time series of the mass flux and precipitation rate are shown for the runs with the Smagorinsky and no mixing scheme, in addition to the TKE mixing scheme, in Fig. 3.9. The nonmonotonic dependence of the mass flux on resolution described above for the TKE scheme also occurs with the Smagorinsky mixing scheme. Moreover, note that there is almost no mass flux for the first half of the simulation in the $\Delta x = 4$ km with the Smagorinsky mixing scheme. With no mixing, the $\Delta x = 4$ km simulation has more mass flux than the 250 m simulations, which is different from the TKE and Smagorinsky cases. The precipi-

tation rates are similarly insensitive to the resolution for the Smagorinsky and no mixing simulations as described above for the TKE case, except for the Smagorinsky scheme with $\Delta x = 4$ km, for which there is no precipitation in the first half of the simulation.

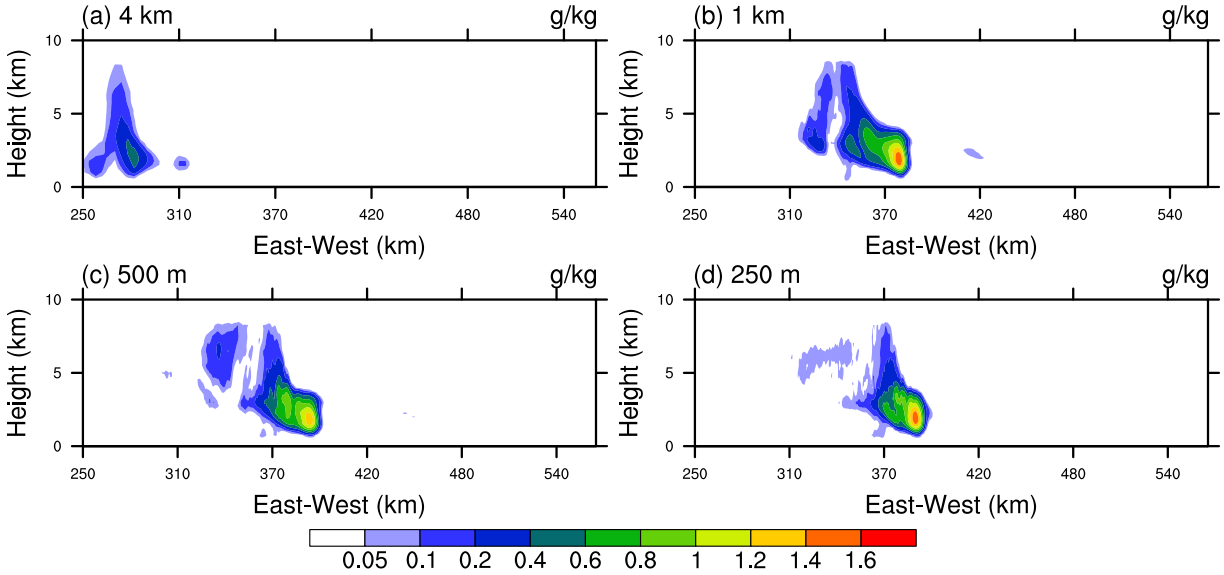

Figure 3.11: Spanwise (y) averaged cloud water mixing ratio for the Smagorinsky simulation with resolutions $\Delta x =$ (a) 4 km, (b) 1 km, (c) 500 m, and (d) 250 m at 240 minutes. For clarity, only the right half of the domain is shown.

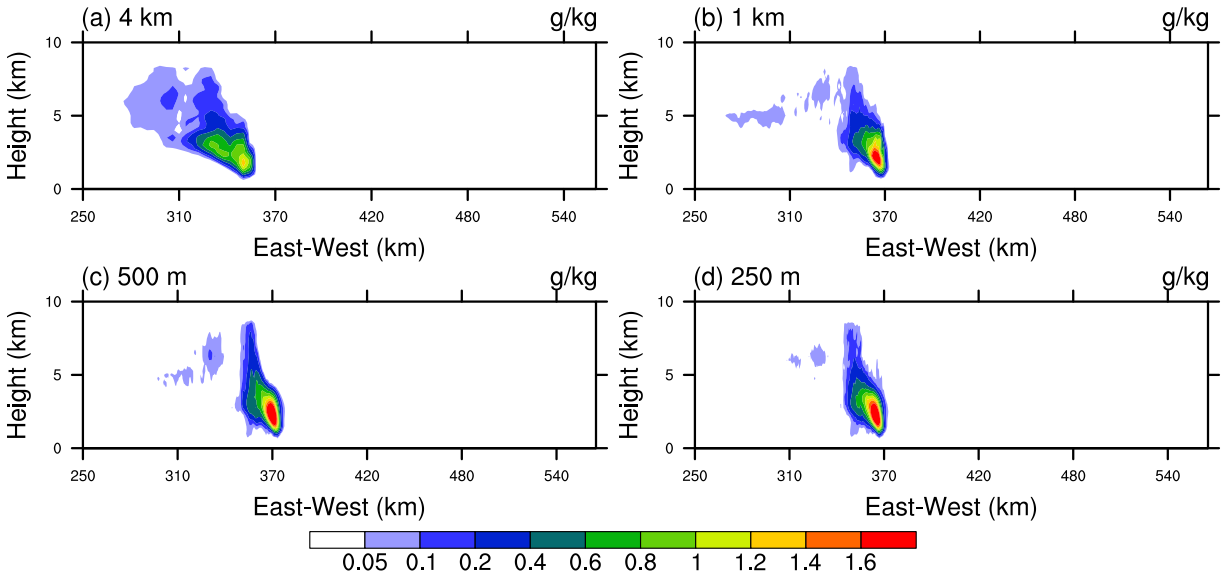

Figure 3.12: Spanwise (y) averaged cloud water mixing ratio for the no subgrid mixing simulation with resolutions Δx = (a) 4 km, (b) 1 km, (c) 500 m, and (d) 250 m at 240 minutes. For clarity, only the right half of the domain is shown.

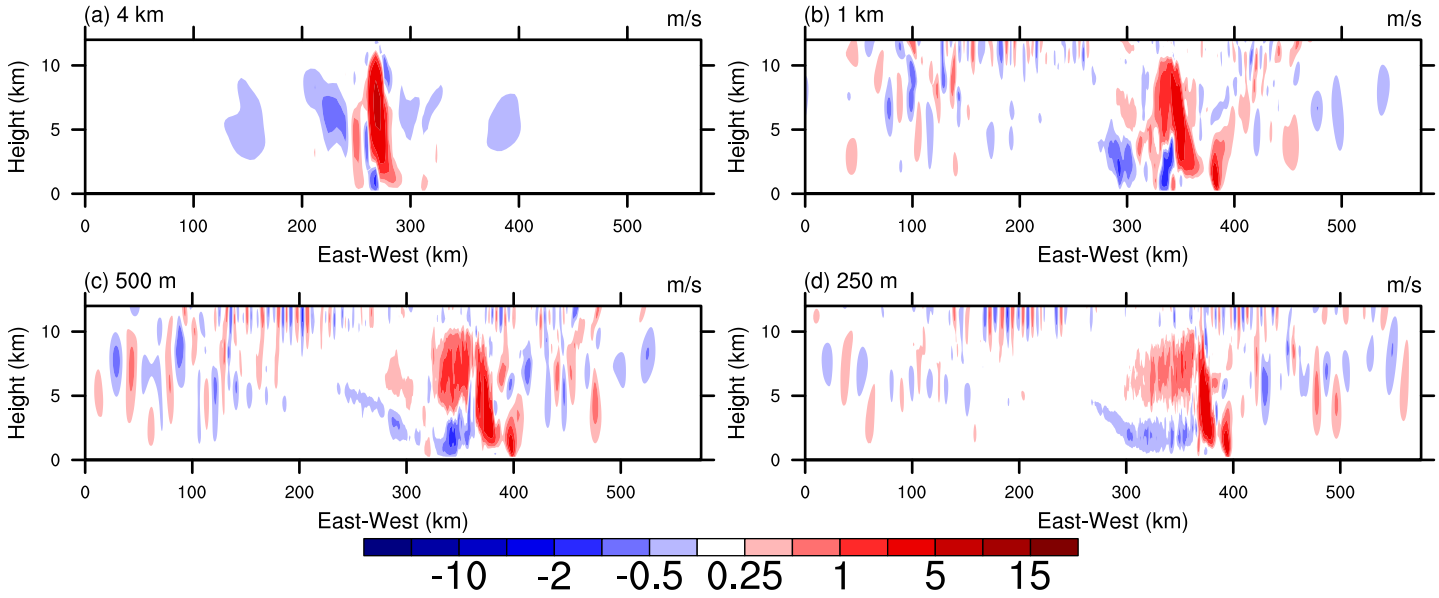

Figure 3.13: Spanwise (y) averaged vertical velocity for the Smagorinsky simulation with resolutions Δx = (a) 4 km, (b) 1 km, (c) 500 m, and (d) 250 m at 240 minutes.

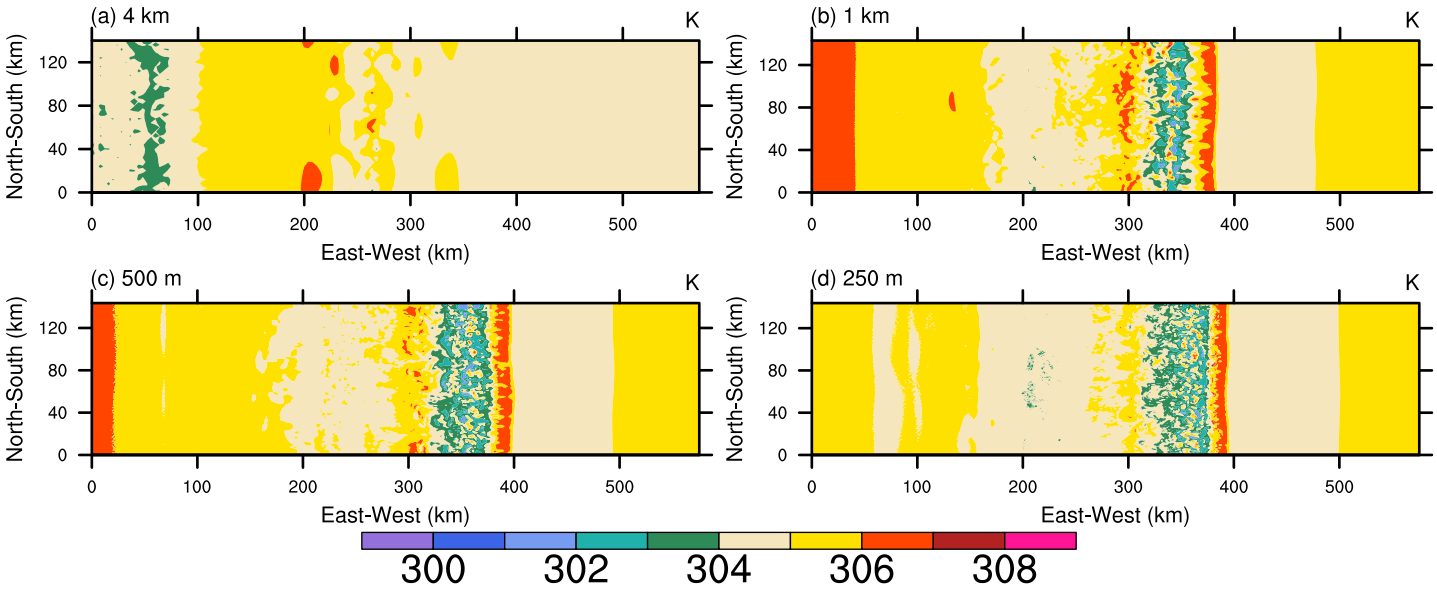

Figure 3.14: Horizontal slice of potential temperature at height of 2 km for the Smagorinsky simulation with resolutions Δx = (a) 4 km, (b) 1 km, (c) 500 m, and (d) 250 m at 240 minutes.

3.4 Effects of Small Scales

3.4.1 Filtered fields

In order to assess the quality of the low resolution simulations, a box-filter is applied to the highest resolution ($\Delta x = 250$ m) simulation with the TKE scheme to compare it with the lower resolution simulations at the same effective resolutions. A two-dimensional horizontal box-filter is used, which applies in the x- and y-directions. A two-dimensional horizontal box-filter is used here in order to investigate the dependence on horizontal resolution of the idealized squall line. The two-dimensional filter can help us to compare filtered high resolution field and unfiltered low resolution field at the same effective horizontal resolution.Filter scales of 500 m, 1 km and 4 km are used. The filtered potential temperature field at $z = 2$ km at 240 minutes are compared.

With a filter scale of 500 m (Fig. 3.15a), the details of the potential temperature slice are similar to the unfiltered $\Delta x = 500$ m case (Fig. 3.15d). However, there are some differences. In the filtered high resolution simulation, the warm leading edge is smaller and there is more small scale turbulence. The reduced turbulent mixing in the warm leading front in the $\Delta x = 500$ m simulation may also explain the delay of the storm development.

With a filter scale of 1 km, the filtered potential temperature (Fig. 3.15b) shown similar details to the 500 m unfiltered simulation (Fig. 3.15e). The linear spanwise structure seen in the $\Delta x = 1$ km simulation (Fig. 3.15e) do not appear in the filtered high resolution simulation, suggesting that these structures are due to the subgrid effect of the TKE mixing scheme with $\Delta x = 1$ km.

Finally, with a filter scale of 4 km, the filtered potential temperature (Fig. 3.15c) shows more small scale structures than the unfiltered $\Delta x = 4$ km simulation in the trailing region (Fig. 3.15f). More mixing occurs in the trailing region in the filtered high resolution case (Fig. 3.15a), and the wobbling of the leading front occurs in the filtered cases but not the $\Delta x = 4$ km cases (Fig. 3.15f). The turbulence structure seen in the warm leading front when filtered to 500 m and 1 km (Fig. 3.15a,b) can not be seen when filtered to 4 km (Fig. 3.15c). This suggests that many of the important turbulent structures are smaller than 4 km and hence can not be resolved by the TKE mixing scheme when $\Delta x = 4$ km. Difference in the overall potential temperature between the filtered and unfiltered $\Delta x = 4$ km simulations are significant. The trailing region in the filtered case is significantly warmer than the unfiltered case. These results suggest that the subgrid turbulence scheme is not able to reproduce the correct potential temperature structure in the trailing turbulent region at resolution $\Delta x = 4$ km. There are clearly some mechanisms that are important for the evolution of the squall line that can not be properly resolved with $\Delta x = 4$ km.

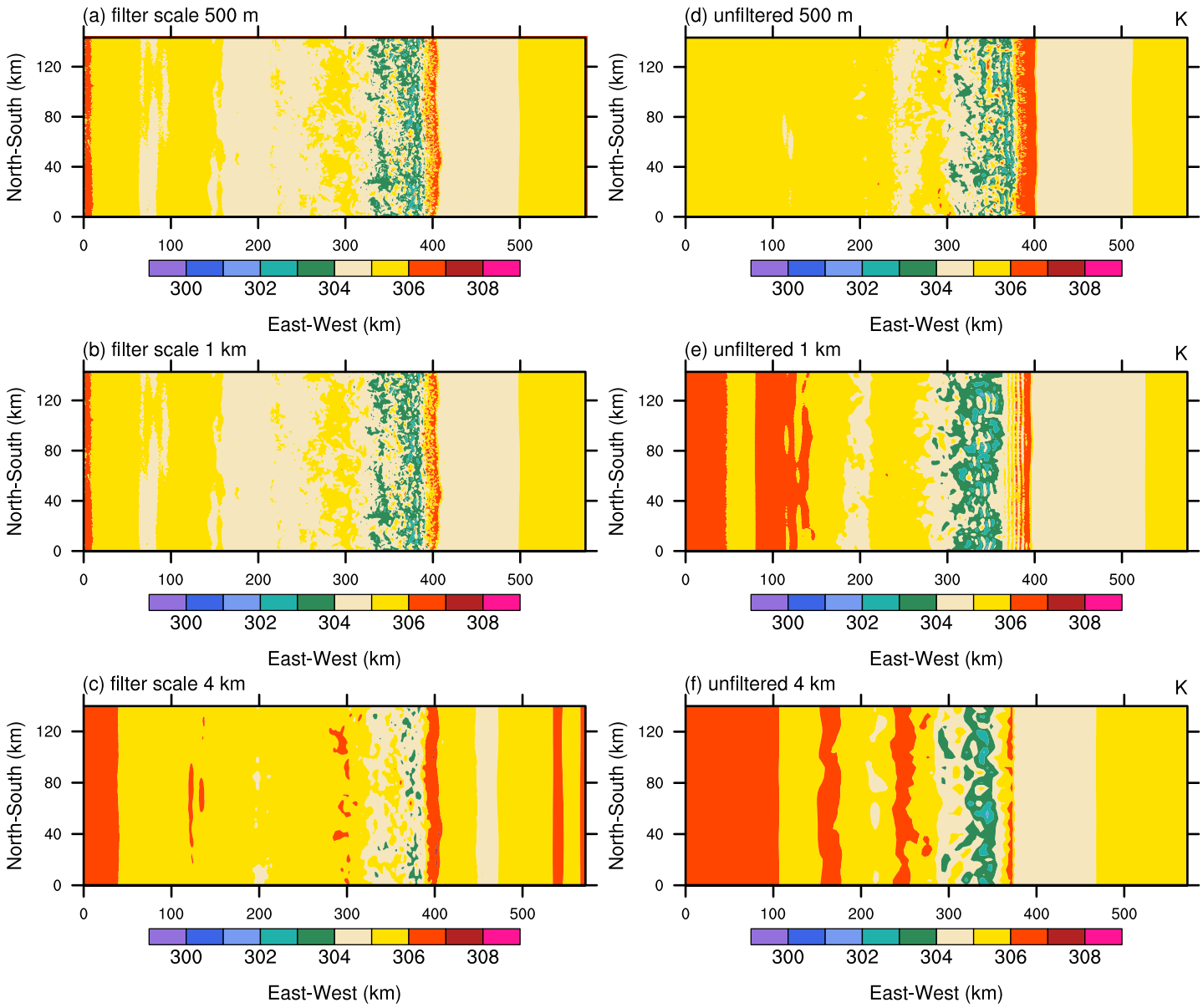

Figure 3.15: Horizontal slices of filtered potential temperature at height of 2 km at 240 minutes for the TKE simulation with $\Delta x = 250$ m filtered to scale of $\Delta x =$ (a) 500 m, (b) 1 km, and (c) 4 km. The slices on the right are the horizontal slices of unfiltered potential temperature at height of 2 km at 240 minutes for the TKE simulation with $\Delta x =$ (d) 500 m, (e) 1 km and (f) 4 km

3.4.2 Subfilter Energy Transfer Rate

The subfilter energy transfer rate has been an active research topic for the community (e.g. [29, 25, 17]). The filtered data is also used for a priori analysis of the effects of the small-scale turbulence in the highest resolution simulation. To better understand the small scale turbulence transfer of the kinetic energy to smaller scales, we filter the model velocity fields in the highest resolution TKE simulation and compute the rate of energy transfer from large to sub-filter scales. When averaged over large areas, the dissipation ϵ_- is expected to dominate over the backscatter ϵ_+, giving a net downscale energy transfer. However, backscatter may be important locally (e.g. [29]) and its structure may point to regions where the eddy viscosity model is particularly problematic.

Figure 3.16 shows the horizontally averaged backscatter and dissipation of the simulation with TKE mixing with $\Delta x = 250$ m filtered to 1 km. Dissipation and backscatter are computed at $z = 2.5$ km, over which the average is taken. The height of 2.5 km is chosen because the cloud water mixing ratio is highest here. The dissipation and backscatter are both significant. The dissipation dominates in the first half of the simulation time, and the backscatter dominates in the second half of the simulation. The dominance of the dissipation at the early stage suggests that the net energy transfer at scale of 1 km is downscale, which is broadly consistent with an eddy viscosity approach; however, the eddy viscosity can not represent the smaller but significant backscatter (especially at later times) that is found.

Figure 3.17 shows the horizontal averaged backscatter and dissipation of the simulation with TKE mixing with $\Delta x = 250$ m filtered to a large scale of 4 km. In this case, the backscatter is more than the energy dissipation at most times, which is not consistent with a downscale cascade or eddy viscosity approach. This finding gives further evidence that $\Delta x = 4$ km is not suitable for large eddy simulation of mesoscale convective systems. Moreover, while the magnitudes of the dissipation rate are similar at scales of 1 km and 4 km, the magnitude of the backscatter at scales of 4 km case is double that of the 1 km case. Also note that Fig. 3.16 and 3.17 show the backscatter and dissipation at height of 2.5 km. In earlier stages of the storm, when updrafts are going through the layer at 2.5 km, the fluctuations of the backscatter and dissipation are significant. Furthermore, note that Figs. 3.16 and 3.17 are similar in the second half of the simulation time. This result suggests that after the storm is fully developed, there is a significant amount of backscatter which provides additional energy to sustain the storm.

Figure 3.18 shows the spanwise averaged subfilter energy transfer rate at 240 minutes, computed using a filter scale of 1 km. The transfer has a very coherent spatial structure. The backscatter is mainly found in the upper convective region and the dissipation is

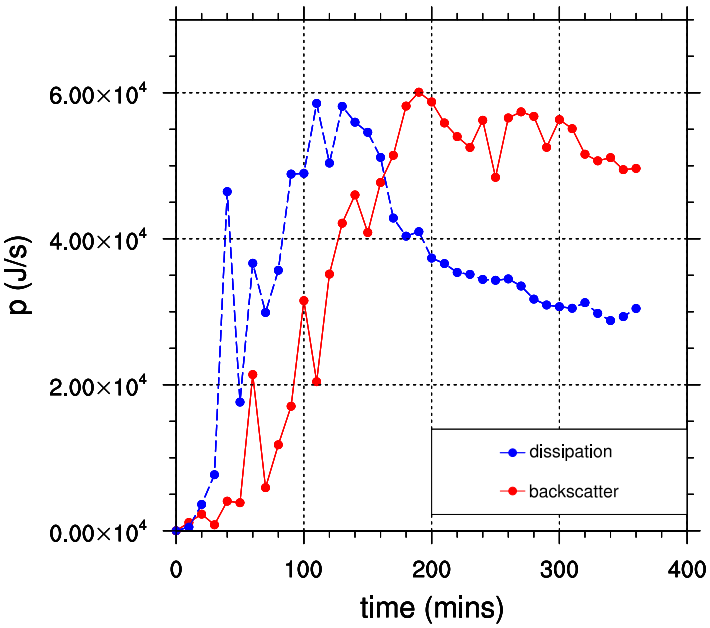

Figure 3.16: Backscatter and dissipation at $z = 2.5$ km when filtered to 1 km.

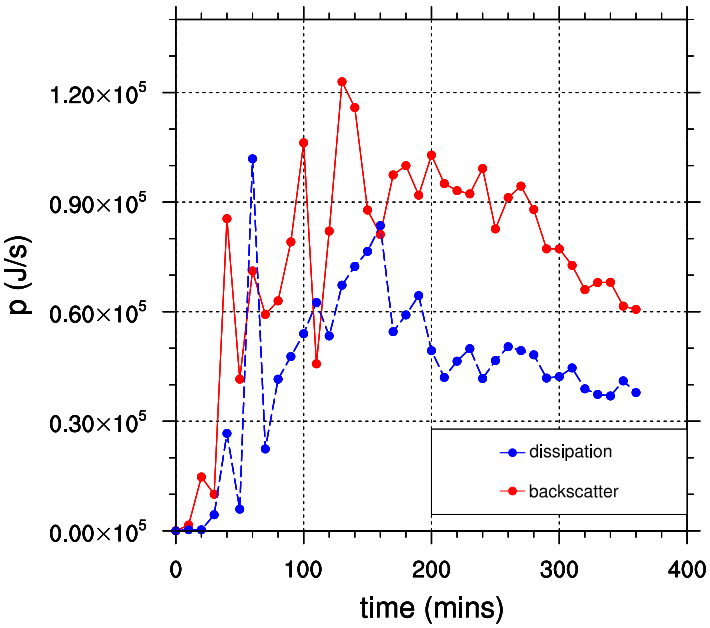

Figure 3.17: Backscatter and dissipation at $z = 2.5$ km when filtered to 4 km.

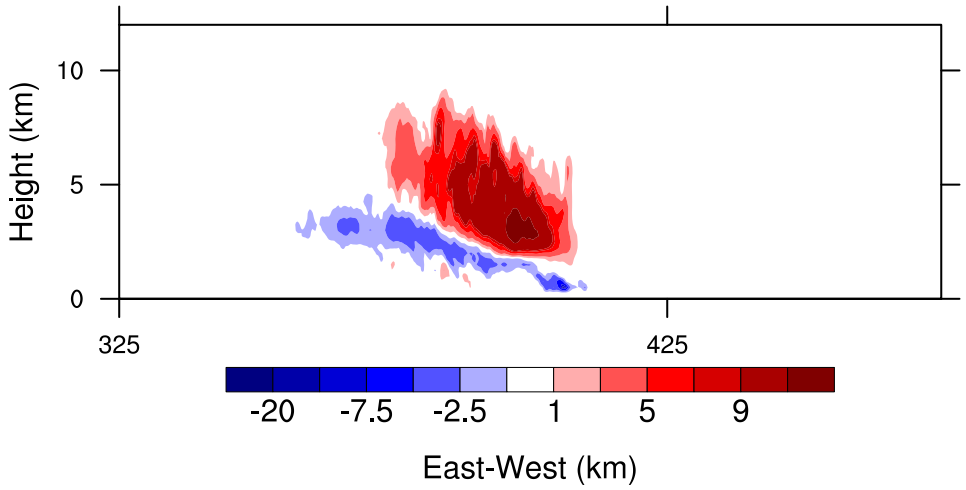

Figure 3.18: Spanwise averaged subfilter energy transfer rate at 240 minutes when filtered to 1 km (x 10^5 J/s).

mainly found in the lower cold pool region. The tilted structure is also very similar to the overall structure shown in the vertical velocity (Fig. 3.7) and cloud water mixing ratio profile (Fig. 3.6). The subfilter energy transfer rate profile is interesting when one compares Fig. 3.18 to Fig. 3.7, as the dissipation is associated with the lower region of the storm and the backscatter is associated with the updraft.

3.4.3 Subgrid TKE Ratio

Following the diagnostic from section 2.3, we consider the subgrid TKE to total TKE ratio R in the simulations with the TKE subgrid mixing scheme. Figure 3.19 shows the spanwise averaged ratio R at 240 minutes. The subgrid TKE is mainly localized in the updraft portion of the storm. Note that the subgrid TKE ratio is significantly higher in the $\Delta x = 4$ km and 1 km cases than the $\Delta x = 500$ m and 250 m cases. At a fixed resolution, high subgrid TKE ratio occurs mainly at the leading front.

Figure 3.20(b) shows the vertical profile of the horizontal averaged subgrid TKE and Fig. 3.20(c) shows the vertical profile of the horizontal averaged subgrid TKE ratio at 180 minutes.

Figure 3.20(b) shows the vertical profile of horizontally averaged subgrid TKE at 180 minutes. Overall, all the profiles with different resolutions have a similar bell shape. The

subgrid TKE decreases with increasing resolution, as expected, and is peaked in all cases at a height of around 2.5 km. A spike occurs around the cloud top for the two highest resolutions. A similar spike was found by Verrelle et al. [40], who suggested that subgrid TKE can be produced by dynamical production and thermal production. Dynamical production is associated with the subgrid TKE generated by shear and friction and thermal production is associated with the subgrid TKE generated by buoyancy [40]. In particular, Verrelle et al. [40] also found evidence that the production of subgrid TKE due to dynamical production is associated with higher resolution, such as horizontal grid spacing of 500 m and 250 m. As a result, a possible source of the spike in the 500 m and 250 m simulations from 3.20(b) can be due to dynamical production of subgrid TKE.

As shown in Fig. 3.20(c) the subgrid TKE ratio is significantly higher for 4 km and 1 km than the 500 m and 250 m cases. At low resolution, the subgrid turbulence scheme is creating more subgrid TKE to compensate for the insufficient resolved turbulence, as expected. Overall, the largest subgrid TKE ratio at each resolution occurs at a height below 5 km. More turbulence occurs at heights below 5 km, due to the interaction between the environmental wind shear and the main updraft.

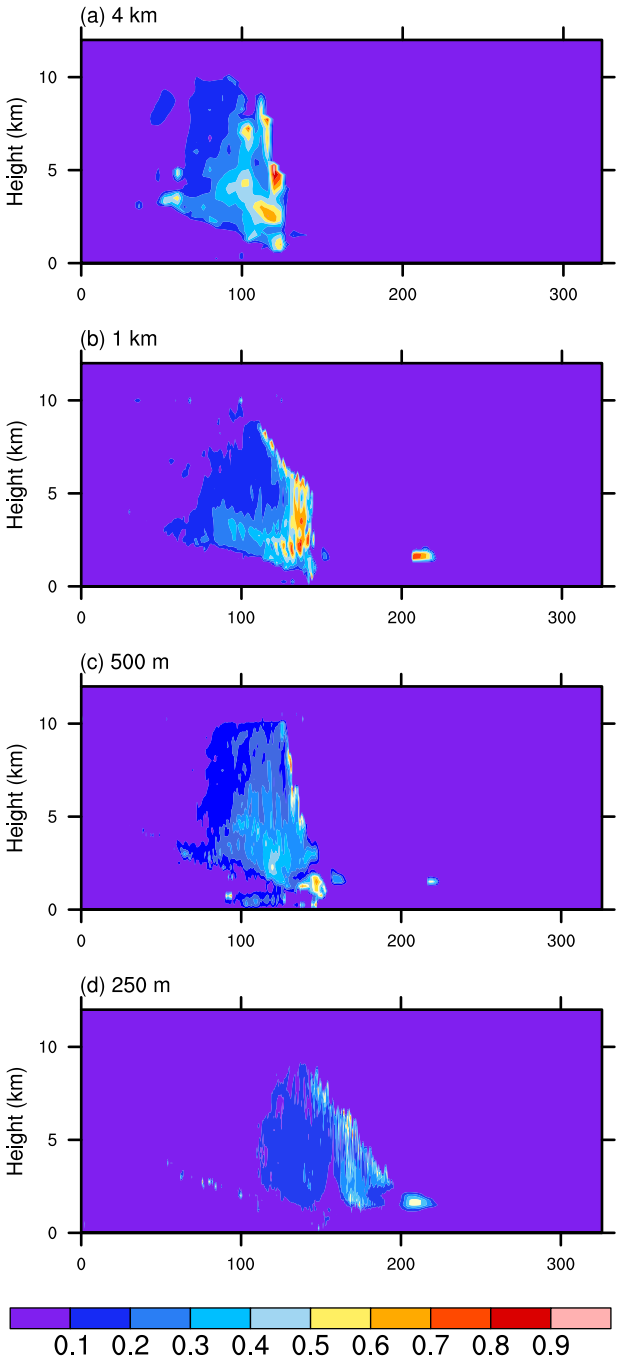

Figure 3.19: Spanwise averaged subgrid TKE ratio R at 240 minutes for TKE simulations with $\Delta x =$ (a) 4 km, (b) 1 km, (c) 500 m, and (d) 250 m. The same figure for Smagorinsky simulations is shown in Fig. 3.22.

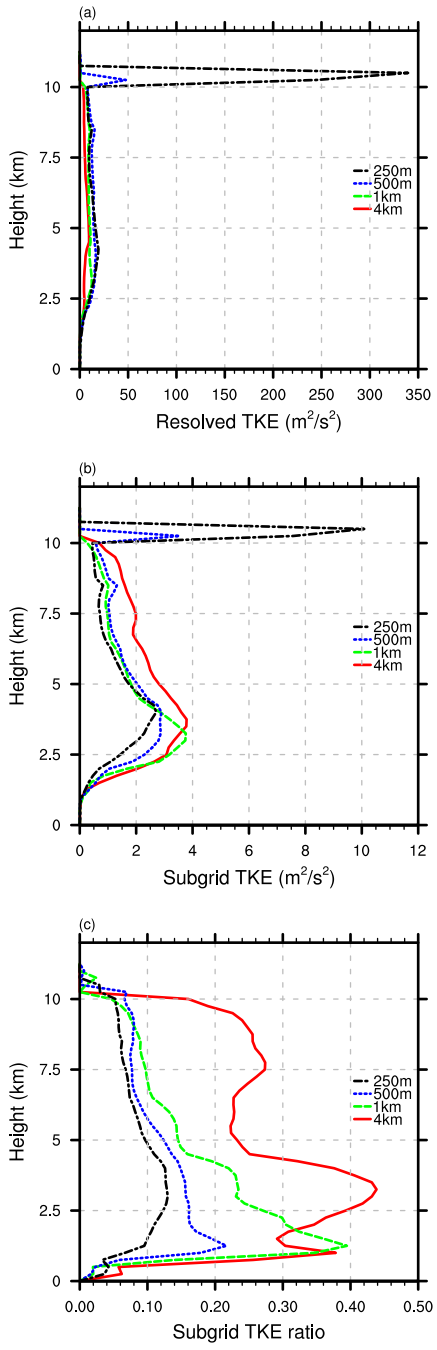

Figure 3.20: (a) Horizontal averaged resolved TKE with height at 180 minutes; (b) Horizontal averaged subgrid TKE with height at 180 minutes; (c) Horizontal averaged subgrid TKE ratio R with height at time 180 minutes; with $\Delta x = 4$ km (red), 1 km (green), 500 m (blue), and 250 m (black).

3.4.4 Smagorinsky Scheme

For comparison, the vertical velocity kinetic energy spectra, the subgrid TKE ratio and the subfilter energy transfer are also computed for simulations with the Smagorinsky scheme. The energy spectra for the Smagorinsky scheme are also very noisy. For the low and medium resolution, there is less energy at large k. Note that the TKE simulation spectra (Fig. 3.10) is closer to a -5/3 power law than the Smagorinsky spectra (Fig. 3.21). The slope of the spectrum with $\Delta x = 250$ m is slightly shallower than the -5/3 line. Overall, similar to the TKE spectra, at the resolution of 4 km, the most energetic convective plumes are not resolved properly, and hence $\Delta x = 4$ km is not recommended based on the vertical velocity kinetic energy spectra for the Smagorinsky scheme.

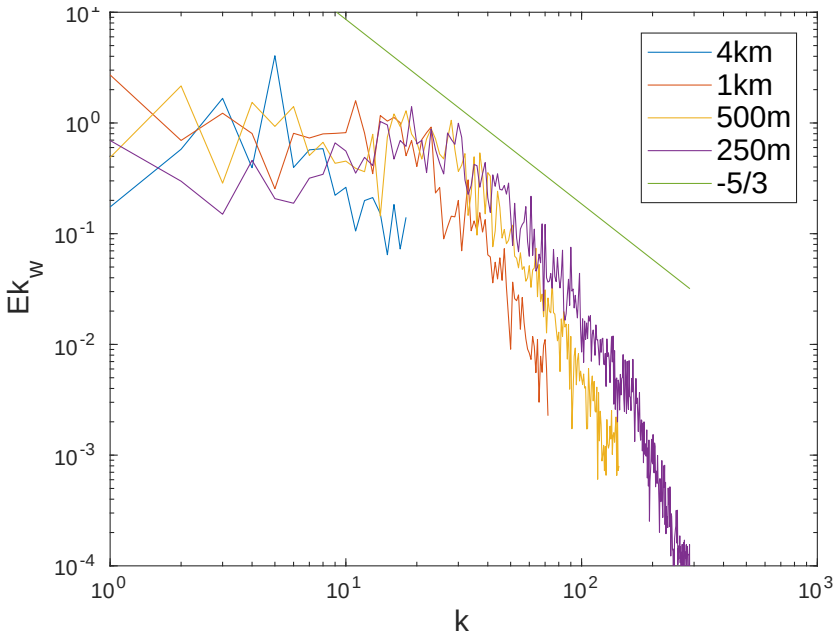

Figure 3.21: One dimensional (spanwise) vertical velocity kinetic energy spectrum at height of 5 km and x of maximum variance [9] for Smagorinsky simulations at resolutions 4 km, 1 km, 500 m, and 250 m. Wavenumbers are nondimensional, so $k = 1$ corresponds to the wavelength of the spanwise domain size 144 km. The green line has a slope of -5/3.

The subgrid TKE field is not used by the Smagorinsky scheme, but the effective TKE can be derived from the Smagorinsky eddy viscosity by comparing (1.37) and (1.39), as

$$e_{SMA} = \left(\frac{K}{\Delta x C_u} \right)^2 ,$$

where K is the horizontal Smagorinsky eddy viscosity and $C_u = 0.15$ is a constant given by the TKE scheme. Figure 3.22, shows the equivalent subgrid TKE ratio for the Smagorinsky simulations. The ratios are significantly larger than those from the TKE simulations (Fig. 3.19). Large amounts of the subgrid TKE can be found in the leading updraft regions. The area with high subgrid TKE ratio decreases in size as resolution increases. Once again, the Smagorinsky scheme is not recommended for resolution lower than $\Delta x = 500$ m, since there are large regions with very high subgrid TKE ratio with values of nearly 1. Such a result suggests that the updraft region of the simulated squall lines in the simulation with resolution lower than $\Delta x = 500$ m is poorly resolved since the turbulence is dominated by subgrid (parameterised) eddies. This finding goes against the fundamental assumptions of LES, in which that the largest eddies are resolved.

In addition, Fig. 3.23 shows the horizontally averaged backscatter and dissipation from the Smagorinsky simulation with $\Delta x = 250$ m filtered to a scale of 1 km at height $z = 2.5$ km. The dissipation and backscatter are both significant. Unlike the results with the TKE scheme (Fig. 3.16), the dissipation dominates over most of the simulation time, but the amount of backscatter is almost half of the dissipation, which is also significant. Overall, the horizontally averaged backscatter and dissipation with filter scale of 1 km obtained with the TKE (Fig. 3.16) and Smagorinsky (Fig. 3.23) schemes are fundamentally different. The dissipation for the Smagorinsky scheme with a filter scale of 1 km dominates over most of the simulation time, while the dissipation for the TKE scheme with a filter scale of 1 km only dominates for the first half of the simulation time. Figure 3.24 shows the same quantity with a filter scale of 4 km. In agreement with the TKE results (Fig. 3.17), the backscatter dominates over dissipation at most times, which is not consistent with the downscale cascade or eddy viscosity approach. This finding gives further evidence that $\Delta x = 4$ km is not suitable for either TKE or Smagorinsky scheme for large eddy simulations of mesoscale convective systems.

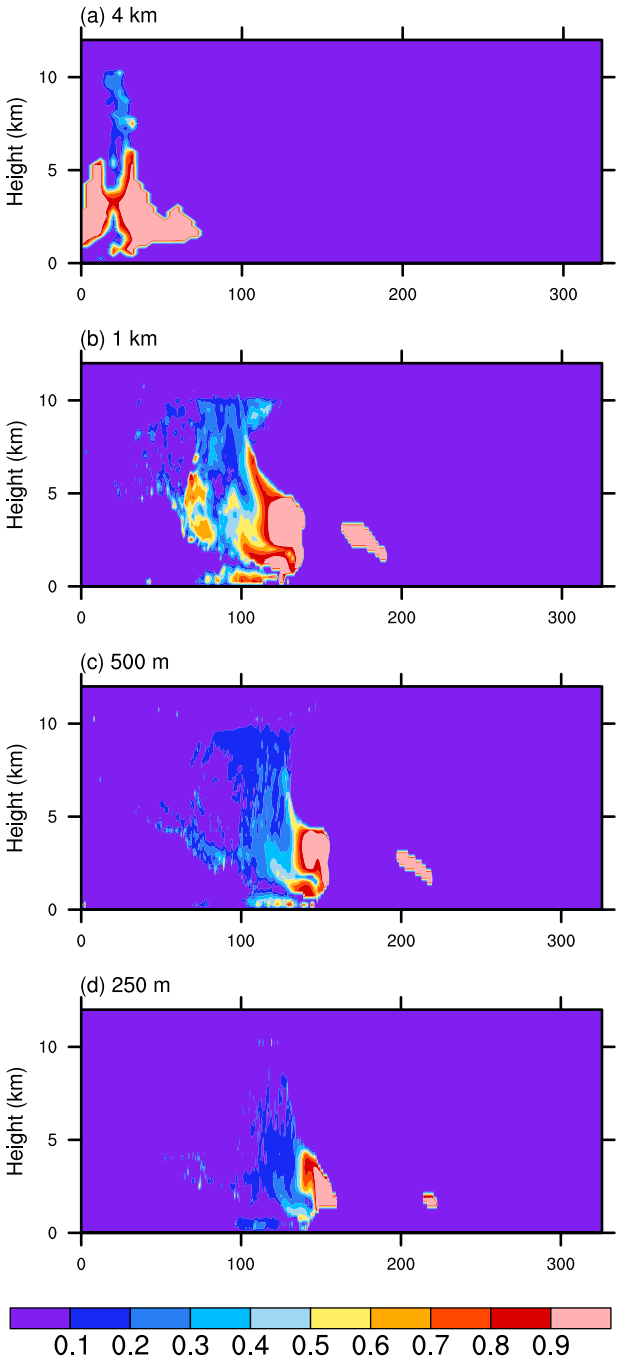

Figure 3.22: Spanwise averaged subgrid TKE ratio R at 240 minutes for Smagorinsky simulations for $\Delta x =$ (a) 4 km, (b) 1 km, (c) 500 m, and (d) 250 m.

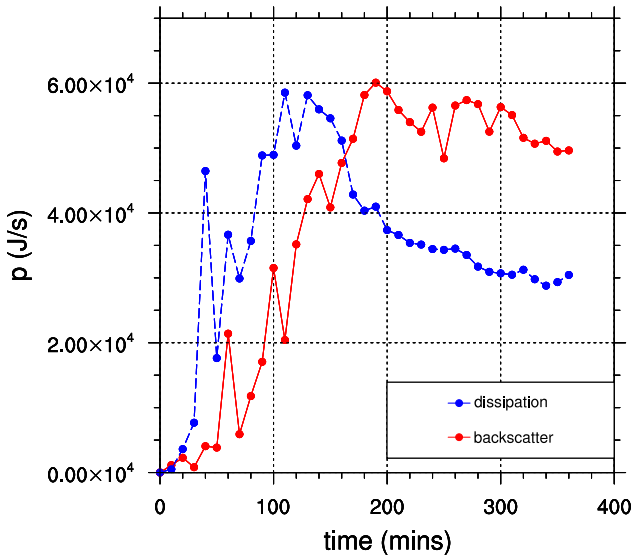

Figure 3.23: Backscatter and dissipation at $z = 2.5$ km when filtered to 1 km for Smagorinsky mixing scheme.

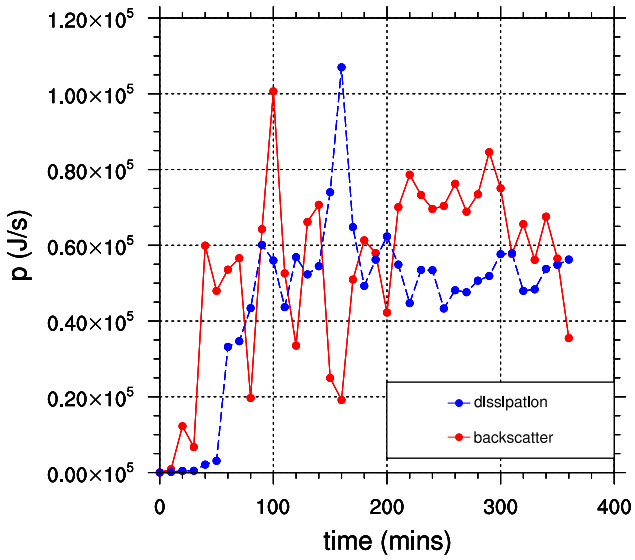

Figure 3.24: Backscatter and dissipation at $z = 2.5$ km when filtered to 4 km for Smagorinsky mixing scheme.

Chapter 4

Summary and Conclusions

4.1 Summary

Overall, all the simulations presented in this thesis are able to produce squall lines with trailing stratiform precipitation within six hours of simulation time. The squall lines are backward tilted, which is the textbook form of the squall lines in shallow shear environments (e.g. [23]). All the simulations are able to produce mature squall lines by about 90 minutes, except the case with $\Delta x = 4$ km and the Smagorinsky scheme.

The effects of horizontal resolution are investigated mainly with the TKE scheme. Overall, the squall lines simulated in this theses are sensitive to resolution. Although the general shape of the squall line is consistent in all simulations, the structural details provided by the simulation with $\Delta x = 4$ are different from those at higher resolution. Squall lines simulated at higher resolution shows more detail in structures. There is a dependence of the individual cell size and cell numbers on resolution, which is also suggested by [20]. The cloud top heights for all simulations are about 10 km and there is no obvious dependence on resolutions or subgrid schemes. Squall lines in simulations with lower resolution often have delayed three-dimensionalisation. At the earlier stage of the simulations (i.e. $t = 90$ minutes), the warm leading front of the simulated squall line with lower resolution has a less turbulent warm leading front than with higher resolution simulation. At a later time, the warm leading front of the low resolution case also become turbulent, which indicates that the three-dimensional mixing is delayed due to the low resolution. The mass flux and precipitation rate do not converge as Δx approaches 250 m, which suggested that the resolution higher than $\Delta x = 250$ m is needed for convergence. The vertical velocity kinetic energy spectra also suggest that grid spacing of 4 km is not sufficient, and even 1 km can

barely resolve the largest turbulent eddies of the squall line. From these results, although it is still unclear what is the best resolution for a simulation of a squall line, the horizontal resolution of 4 km should clearly not be used for simulations for squall lines or likely other simulations of mesoscale convective systems.

In addition, simulated squall lines are sensitive to subgrid mixing schemes at a fixed resolution. As mentioned above, only the simulation with $\Delta x = 4$ km and the Smagorinsky scheme can not produce a squall line properly in the first half of the simulation time. The development of the squall line in that simulation is significantly delayed. Moreover, at the same resolution, the Smagorinsky scheme simulations do not show the same level of detailed structure as the simulations with the TKE scheme in fields such as cloud water mixing ratio, potential temperature and vertical velocity. The propagation speed of the squall lines simulated with the Smagorinsky scheme is also slower than that obtained with the TKE scheme at the same resolution. Overall, the TKE scheme gives superior results to the Smagorinsky scheme at the same resolution.

The effects of small scales are also used to evaluate the effectiveness of a particular resolution in resolving the small scale structures of the simulated squall line. The filtered potential temperature, subgrid TKE ratio and the subfilter energy transfer are used for the evaluations. Comparing the results from the filtered and unfiltered potential temperature, we learn that the low resolution unfiltered simulation ($\Delta x = 4$ km) is missing some important large scale mixing mechanisms. Comparing the filtered potential temperature at different filter scales can also tell us how important mixing is at a particular resolution. The subgrid TKE ratio decreases as the resolution increases, as expected. High values of subgrid TKE ratio are mainly localized in the leading updraft regions of the squall lines. Furthermore, significant backscatter occurs at $z = 2.5$ km for the high resolution simulation filtered to scales of 1 km and 4 km. In fact, the dissipation is less than the backscatter in most of the simulation time for filter scale of $\Delta x = 4$ km, and during the second half of the simulation time for the simulation with filter scale of $\Delta x = 1$ km. The backscatter occurs mainly in the upper region of the squall line, and the dissipation occurs mainly in the lower region.

4.2 Conclusions

Resolution has great effects on idealized squall lines simulations from $\Delta x = 4$ km to 250 m. With TKE mixing, while $\Delta x = 4$ km is able to produce the general structures of the squall line, higher resolution simulations are able to produce more details shown in the structures of the storms, in agreement with previous studies (e.g. [9, 8]). Horizontal resolution of

1 km with TKE mixing produces trailing banded clouds, which has not been reported in previous studies. These banded structures do not occur at lower or higher resolution. Moreover, the higher resolution (Δx = 250 and 500 m) is able to produce squall lines with smaller and more separated convective structures (e.g. [9, 8, 40]). Low resolutions lead to longer time to three-dimensionalize and hence delay the development of the storm, also in agreement with previous studies (e.g. [9]). From the energy spectra, $\Delta x = 4$ km is not enough to resolve the largest turbulent eddies. Although resolution has significant effects on many aspects of the squall line, cloud top height does not change significantly as the resolution increases, in contrast with other studies (e.g. [42, 8]). This result may due to difference in the sounding profile, since idealized storm simulations are known to be sensitive to environmental conditions [27]. While the subgrid TKE ratio decreases as the resolution increases, in agreement with [9], it is still unclear why contrasting results were given from studies such as [2, 39].

Significant amounts of backscatter exist across filter scales of 4 km and even 1 km. This backscatter can not be represented by eddy viscosity models such as the Smagorinsky and TKE scheme. Again, these subfilter energy transfers confirm that $\Delta x = 4$ km is not suitable for a squall line simulation. In fact, they suggest that $\Delta x = 1$ km is also not ideal for a squall line simulation because of the backscatter at this scale, even though it is better than $\Delta x = 4$ km.

At a fixed resolution, the TKE scheme is a better mixing scheme than the Smagorinsky scheme. At the coarsest resolution $\Delta x = 4$ km, the Smagorinsky scheme simulation does not even produce a propagating squall line, but the TKE scheme does. The Smagorinsky scheme is known to be too dissipative [30]. In the $\Delta x = 4$ km case, excessive missing from the Smagorinsky scheme is preventing the squall line from properly developing at the earlier stage. Smagorinsky mixing with the high resolution produce similar results to the lower resolution TKE mixing simulations. As a result, despite the fact that the TKE method is slightly more expensive than Smagorinsky at a fixed resolution, the Smagorinsky scheme requires more computational resources to obtain the same results as the TKE scheme, because it requires higher resolution. Overall, 4 km is not recommended in any mesoscale simulations with explicit convection. A minimum resolution of 250 m is highly recommended for simulations with TKE and Smagorinsky mixing schemes. Despite these findings, simulations with $\Delta x = 4$ km are often used (especially in global simulations) with no convective parameterisation (e.g. [10, 43]).

4.3 Future Work

The potential follow up opportunities in this field are huge. Many of the inconsistencies between the results from this project and previous studies are still not properly addressed. Here are some potential future topics that could be pursued.

4.3.1 CAPE

This project considered a single initial sounding. However, it is known that the characteristics of the sounding profile, such as CAPE and CIN, have a significant effect on the evolution and simulation of squall lines (e.g. [27]). The idealized squall line simulated in this project is placed in a relatively low CAPE environment. The cloud top heights in all simulations are about 10 km with no significant dependence on the resolution, while the cloud top heights from Bryan and Morrison [8] have a nonmonotonic trend as the resolution increases. Such differences may also be due to the fact that a different sounding profile is used. This hypothesis could be investigated by performing additional simulations with different initial soundings.

4.3.2 Wind Shear

Inconsistencies in the subgrid TKE ratio have been reported in the literature, which may be due to the type of wind shear. While Adlerman and Droegemeier [2] and Verrelle et al. [39] found that the subgrid TKE ratio increases as the resolution increases, Bryan et al. [9] and this project found that the subgrid TKE ratio decreases as the resolution increases. In general, one would expect that subgrid TKE ratio decreases as the resolution increases since the smaller scale turbulent eddies generally have less kinetic energy than larger eddies. The main difference between these projects is that Adlerman and Droegemeier [2] and Verrelle et al. [39] considered idealized supercell simulations, while Bryan et al. [9] and this thesis considered idealized simulations of squall lines. The storm is largely determined by the type of wind shear present. A unidirectional wind shear profile is often associated with a squall line and a curved wind shear profile is often associated with a supercell storm. To investigate this hypothesis, the shear profile could be modified, holding other parameters fixed, to determine the effect of the shear and storm type on subgrid TKE ratio.

4.3.3 CFL conditions

The Courant–Friedrichs–Lewy (CFL) conditions for the simulations presented in this project are not the same. The simulations with $\Delta x = 4$ km, 1 km and 500 m use a timestep of 3 seconds, and the simulations with $\Delta x = 250$ m use a timestep of 1 second. Furthermore, the maximum velocities in all cases are different. Different CFL conditions may correspond to the difference in numerical diffusion. The effects of numerical diffusion on idealized simulations for squall lines in this project are unclear and not well-documented. An idealized squall line with $\Delta x = 250$ m has been simulated with the same CFL condition as the $\Delta x = 1$ km case (not shown), and no differences can be seen when comparing the vertical slice of the cloud water mixing ratios. Although this small experiment suggests that no major differences can be seen in the structure of the squall line, some carefully conducted studies would be helpful in confirming that the effects of numerical diffusion are not significant.

4.3.4 Subgrid Mixing Scheme

It is not common for idealized squall line simulations to use mixing schemes other than the Smagorinsky or TKE scheme, because other more advanced schemes are costly computationally. Dynamical reconstruction model (DRM) (e.g. [30]) will be interesting for application in an idealized squall line simulation. The Dynamical Smagorinsky model (e.g. [30]) modifies the k^2 in the Smagorinsky scheme rather than setting it to a constant. The newly derived k^2 can be negative, which allows some backscatter. Theoretically, the dynamical model will be capable of handling backscatter, which the Smagorinsky scheme and TKE scheme are not designed for handling.

References

[1] The NCAR Command Language (version 6.4.0) [software]. 2017. Boulder, Colorado: UCAR/NCAR/CISL/TDD. http://dx.doi.org/10.5065/D6WD3XH5.

[2] E. J. Adlerman and K. K. Droegemeier. The sensitivity of numerically simulated cyclic mesocyclogenesis to variations in model physical and computational parameters. *Monthly Weather Review*, 130(11):2671–2691, 2002.

[3] E. J. Adlerman and K. K. Droegemeier. The dependence of numerically simulated cyclic mesocyclogenesis upon environmental vertical wind shear. *Monthly Weather Review*, 133(12):3595–3623, 2005.

[4] American Meteorological Society. cited 2018: "squall line". *Glossary of Meteorology*. [Available online at http://glossary.ametsoc.org/wiki/].

[5] L. M. Avallone and B. Baeuerle. A 20-year history of NSF-supported atmospheric science field campaigns: statistics and demographics. *Bulletin of the American Meteorological Society*, 98(7):1333–1339, 2017.

[6] S. Bélair and J. Mailhot. Impact of horizontal resolution on the numerical simulation of a midlatitude squall line: Implicit versus explicit condensation. *Monthly Weather Review*, 129(9):2362–2376, 2001.

[7] H. B. Bluestein and M. L. Weisman. The interaction of numerically simulated supercells initiated along lines. *Monthly Weather Review*, 128(9):3128–3149, 2000.

[8] G. H. Bryan and H. Morrison. Sensitivity of a simulated squall line to horizontal resolution and parameterization of microphysics. *Monthly Weather Review*, 140(1):202–225, 2012.

[9] G. H. Bryan, J. C. Wyngaard, and J. M. Fritsch. Resolution requirements for the simulation of deep moist convection. *Monthly Weather Review*, 131(10):2394–2416, 2003.

[10] J. Done, C. A. Davis, and M. Weisman. The next generation of NWP: Explicit forecasts of convection using the Weather Research and Forecasting (WRF) model. *Atmospheric Science Letters*, 5(6):110–117, 2004.

[11] E. Fiori, A. Parodi, and F. Siccardi. Turbulence closure parameterization and grid spacing effects in simulated supercell storms. *Journal of the Atmospheric Sciences*, 67(12):3870–3890, 2010.

[12] W. W. Grabowski. Toward cloud resolving modeling of large-scale tropical circulations: A simple cloud microphysics parameterization. *Journal of the Atmospheric Sciences*, 55(21):3283–3298, 1998.

[13] W. W. Grabowski and P. K. Smolarkiewicz. A multiscale anelastic model for meteorological research. *Monthly Weather Review*, 130(4):939–956, 2002.

[14] R. A. Houze Jr. Mesoscale convective systems. *Reviews of Geophysics*, 42(4), 2004.

[15] R. P. James and P. M. Markowski. A numerical investigation of the effects of dry air aloft on deep convection. *Monthly Weather Review*, 138(1):140–161, 2010.

[16] P. A. Jiménez, J. Dudhia, J. F. González-Rouco, J. Navarro, J. P. Montávez, and E. García-Bustamante. A revised scheme for the WRF surface layer formulation. *Monthly Weather Review*, 140(3):898–918, 2012.

[17] S. Khani and M. L. Waite. Backscatter in stratified turbulence. *European Journal of Mechanics-B/Fluids*, 60:1–12, 2016.

[18] G. Kirkil, J. Mirocha, E. Bou-Zeid, F. K. Chow, and B. Kosović. Implementation and evaluation of dynamic subfilter-scale stress models for large-eddy simulation using WRF. *Monthly Weather Review*, 140(1):266–284, 2012.

[19] P. K. Kundu and I. M. Cohen. *Fluid Mechanics*. Academic Press, second edition, 2001.

[20] Z. Lebo and H. Morrison. Effects of horizontal and vertical grid spacing on mixing in simulated squall lines and implications for convective strength and structure. *Monthly Weather Review*, 143(11):4355–4375, 2015.

[21] D. K. Lilly. K. The representation of small-scale turbulence in numerical simulation experiments. *Proc. IBM Sci. Comput. Symp. on Environm. Sci*, pages 195–210, 1967.

[22] D. K. Lilly. The dynamical structure and evolution of thunderstorms and squall lines. *Annual Review of Earth and Planetary Sciences*, 7(1):117–161, 1979.

[23] Y.-L. Lin. *Mesoscale Dynamics*. Cambridge University Press, 2007.

[24] Y.-L. Lin, R. D. Farley, and H. D. Orville. Bulk parameterization of the snow field in a cloud model. *Journal of Climate and Applied Meteorology*, 22(6):1065–1092, 1983.

[25] C.-H. Moeng. A closure for updraft–downdraft representation of subgrid-scale fluxes in cloud-resolving models. *Monthly Weather Review*, 142(2):703–715, 2014.

[26] C.-H. Moeng, P. Sullivan, M. Khairoutdinov, and D. Randall. A mixed scheme for subgrid-scale fluxes in cloud-resolving models. *Journal of the Atmospheric Sciences*, 67(11):3692–3705, 2010.

[27] H. Morrison, A. Morales, and C. Villanueva-Birriel. Concurrent sensitivities of an idealized deep convective storm to parameterization of microphysics, horizontal grid resolution, and environmental static stability. *Monthly Weather Review*, 143(6):2082–2104, 2015.

[28] K. Peters and C. Hohenegger. On the dependence of squall-line characteristics on surface conditions. *Journal of the Atmospheric Sciences*, 74(7):2211–2228, 2017.

[29] U. Piomelli, W. H. Cabot, P. Moin, and S. Lee. Subgrid-scale backscatter in turbulent and transitional flows. *Physics of Fluids A: Fluid Dynamics*, 3(7):1766–1771, 1991.

[30] S. B. Pope. *Turbulent Flows*. Cambridge University Press, 2000.

[31] C. K. Potvin and M. L. Flora. Sensitivity of idealized supercell simulations to horizontal grid spacing: Implications for warn-on-forecast. *Monthly Weather Review*, 143(8):2998–3024, 2015.

[32] R. Rogers and M. K. Yau. *A Short Course in Cloud Physics*. Elsevier, 1996.

[33] R. Rotunno, J. B. Klemp, and M. L. Weisman. A theory for strong, long-lived squall lines. *Journal of the Atmospheric Sciences*, 45(3):463–485, 1988.

[34] L. Schlemmer and C. Hohenegger. The formation of wider and deeper clouds as a result of cold-pool dynamics. *Journal of the Atmospheric Sciences*, 71(8):2842–2858, 2014.

[35] W. C. Skamarock, J. B. Klemp, J. Dudhia, D. O. Gill, D. M. Barker, M. G. Duda, X.-Y. Huang, W. Wang, and J. G. Powers. A description of the advanced research WRF version 3. Technical report, National Center For Atmospheric Research Boulder Co Mesoscale and Microscale Meteorology Div, 2008. NCAR Tech. Note NCAR/TN-475+STR, 113 pp. doi:10.5065/D68S4MVH.

[36] J. Smagorinsky. General circulation experiments with the primitive equations: I. The basic experiment. *Monthly Weather Review*, 91(3):99–164, 1963.

[37] T. Takemi and R. Rotunno. The effects of subgrid model mixing and numerical filtering in simulations of mesoscale cloud systems. *Monthly Weather Review*, 131(9):2085–2101, 2003.

[38] G. Vallis. *Atmospheric and Oceanic Fluid Dynamics: Fundamentals and Large-Scale Circulation*. Cambridge University Press, 2006.

[39] A. Verrelle, D. Ricard, and C. Lac. Sensitivity of high-resolution idealized simulations of thunderstorms to horizontal resolution and turbulence parametrization. *Quarterly Journal of the Royal Meteorological Society*, 141(687):433–448, 2015.

[40] A. Verrelle, D. Ricard, and C. Lac. Evaluation and improvement of turbulence parameterization inside deep convective clouds at kilometer-scale resolution. *Monthly Weather Review*, 145(10):3947–3967, 2017.

[41] M. L. Waite. Dependence of model energy spectra on vertical resolution. *Monthly Weather Review*, 144(4):1407–1421, 2016.

[42] M. L. Waite and B. Khouider. The deepening of tropical convection by congestus preconditioning. *Journal of the Atmospheric Sciences*, 67(8):2601–2615, 2010.

[43] M. L. Weisman, C. Davis, W. Wang, K. W. Manning, and J. B. Klemp. Experiences with 0–36-h explicit convective forecasts with the WRF-ARW model. *Weather and Forecasting*, 23(3):407–437, 2008.

[44] M. L. Weisman and J. B. Klemp. The dependence of numerically simulated convective storms on vertical wind shear and buoyancy. *Monthly Weather Review*, 110(6):504–520, 1982.

[45] M. L. Weisman, W. C. Skamarock, and J. B. Klemp. The resolution dependence of explicitly modeled convective systems. *Monthly Weather Review*, 125(4):527–548, 1997.

[46] J. Wyngaard. *Turbulence in the Atmosphere*. Cambridge University Press, 2010.

APPENDICES

Appendix A

High Performance Computing

In this thesis, all the simulations are performed using the Sharcnet Graham supercomputers. Graham has 36160 CPU cores and 320 GPUs. Intel E5-2683 V4 CPUs @ 2.1 GHz are used in most of the nodes. Nvidia Tesla P100 GPUs are used in Graham.

The number of cores and time required for the simulations are shown in Table A.1. Note that the simulation time required for different schemes are similar at a fixed resolution.

Δx (m)	Number of Cores Used	Time Used
250	256	2 days and 6 minutes
500	256	3 hours and 56 minutes
1000	16	5 hours and 34 minutes
4000	16	18 minutes

Table A.1: List of CPU time.